

# **Circumstellar Envelopes of Stars on the Asymptotic Giant Branch**

The determination of gas mass-loss rates, identification of molecules and detection of dust

Bachelor's thesis at Department of Space, Earth and Environment

Marcus Alm, Gabriel Angerd, Tomas Lundberg,  
Sebastian Oleszko, Alexander Wölfinger

BACHELOR'S THESIS 2019:SEEX15-19-80

# Circumstellar Envelopes of stars on the Asymptotic Giant Branch

The determination of gas mass-loss rates, identification of molecules and  
detection of dust

Marcus Alm, Gabriel Angerd, Tomas Lundberg, Sebastian Oleszko,  
Alexander Wölfinger



UNIVERSITY OF  
GOTHENBURG

---



**CHALMERS**  
UNIVERSITY OF TECHNOLOGY

Department of Space, Earth and Environment  
CHALMERS UNIVERSITY OF TECHNOLOGY  
UNIVERSITY OF GOTHENBURG  
Gothenburg, Sweden 2019

Circumstellar Envelopes of stars on the Asymptotic Giant Branch

The determination of gas mass-loss rates, identification of molecules and detection of dust

Marcus Alm, Gabriel Angerd, Tomas Lundberg, Sebastian Oleszko, Alexander Wölfinger

© Marcus Alm, Gabriel Angerd, Tomas Lundberg, Sebastian Oleszko, Alexander Wölfinger, 2019.

Supervisor: Matthias Maercker, Department of Space, Earth and Environment, Elvire de Beck, Department of Space, Earth and Environment

Examiner: Magnus Thomasson, Department of Space, Earth and Environment

Bachelor's Thesis 2019:SEEX15-19-80

Department of Space, Earth and Environment

Chalmers University of Technology

SE-412 96 Gothenburg

Telephone +46 31 772 1000

Cover:  $^{12}\text{CO } J = 3 \rightarrow 2$  emission from the star U Hya.

Typeset in L<sup>A</sup>T<sub>E</sub>X

Printed by Chalmers Reproservice

Gothenburg, Sweden 2019

Circumstellar Envelopes of stars on the Asymptotic Giant Branch

The determination of gas mass-loss rates, identification of molecules and detection of dust

Marcus Alm, Gabriel Angerd, Tomas Lundberg, Sebastian Oleszko, Alexander Wölfinger

Department of Space, Earth and Environment

Chalmers University of Technology

---

## Abstract

Using data observed in Band 6 (211-275 GHz) and Band 7 (275-373 GHz) with the interferometer ACA (part of ALMA) from the DEATHSTAR project [1] we have analysed the CSEs of 5 AGB stars; three carbon-rich (Y Hya, U Hya and R For) and two oxygen-rich (R Hya and R Crt). The analysis was comprised of three main areas: determining the gas mass-loss rates,  $\dot{M}$ , identifying molecules and investigating the presence of dust, where the analysis of  $\dot{M}$  was the most extensive. Using the CO lines  $J = 2 \rightarrow 1$  and  $J = 3 \rightarrow 2$  we determined  $\dot{M}$  with an equation from Ramstedt et al. 2008 [2] based on CO radiative transfer, as well as the expansion velocities of the CSEs. All calculated values of  $\dot{M}$ , ranging  $2.2\text{-}22 \cdot 10^{-7} M_{\odot} \text{yr}^{-1}$  (+79%/ - 66%), were within the equations stated error margin of a factor of three[2] and consistently higher, compared to values in the literature obtained with CO radiative transfer modelling[3, 4]. Due to the equation used for  $\dot{M}$  being based on single-dish telescopes, conversions for our data had to be made. Therefore, a systematic error in the conversion could account for the higher values. Furthermore, the expansion velocities were significantly higher than those in the literature[4] for all stars except Y Hya. However, the data used by us had a higher signal to noise ratio and overall lower uncertainty in comparison[5], indicating that our values may be more accurate. All molecules identified from the frequency spectra in Band 6 (215.4 - 217.4, 217.3-219.3, 230.2-231.2, 231.1-233.1 GHz) and Band 7 (330.3-331.3, 331.3-333.3, 342.5-344.5, 345.1-346.1 GHz), 15 in total with 11 in the carbon stars and 10 in the oxygen stars, were common for the respective spectral type except the recently (2016) discovered AlO [6], which was identified in R Crt. The spectral index,  $\alpha$ , was calculated from the flux in continuum emission in Band 6 (224.3-241.9 GHz) and band 7 (338.2-354.0 GHz). The temperature was calculated for the stars with  $\alpha \approx 2$  (Y Hya and R Crt) and agreed with the temperatures in the literature [3, 4]. For the stars with  $\alpha \neq 2$  (U Hya, R For and R Hya) the dust mass,  $M_D$ , and the dust mass-loss rate,  $\dot{M}_D$ , was calculated with an assumed dust temperature of  $T_{dust} = 100$  K if the measured flux was 10% higher than expected (R For and R Hya), giving the uncertain values (due to  $T_{dust}$  having an exponential relation)  $M_D = 10^{-5} M_{\odot}$  for both stars and  $\dot{M}_D = 10^{-8} M_{\odot} \text{yr}^{-1}$  and  $\dot{M}_D = 10^{-7} M_{\odot} \text{yr}^{-1}$  for R For and R Hya respectively.

---

## Sammandrag

Genom att använda data i Band 6 (211-275 GHz) och Band 7 (275-373) GHz med interferometern ACA (del av ALMA) från DEATHSTAR projektet analyserades CSEer av 5 AGB-stjärnor; tre kolrika (Y Hya, U Hya och R For) och två syrerika (R Hya och R Crt). Analysen bestod av tre huvudområden: bestämma hastigheten för massförlusten av gaser,  $\dot{M}$ , identifiera molekyler och om det fanns stoft, där analysen av  $\dot{M}$  var den mest omfattande. Genom att använda CO linjerna  $J = 2 \rightarrow 1$  och  $J = 3 \rightarrow 2$  bestämdes  $\dot{M}$  med en formel från Ramstedt et al. 2008 [2] baserat på CO-strålningstransport, samt expansionshastigheten för CSEn. Alla beräknade värden för  $\dot{M}$  (som spänner  $2.2-22 \cdot 10^{-7} M_{\odot} yr^{-1}$ ) (+79%/ - 66%) var inom ekvationens givna felmarginaler, en faktor tre[2], jämfört med värden hittad i litteraturen [3, 4] baserade på CO-strålningstransportsmodellering. En möjlig förklaring är att ekvationen för  $\dot{M}$  är framtagen för teleskop med en parabol, vilket gör att konvertering av vår data behövs. Ett systematiskt fel i konverteringen kan därför orsaka de förhöjda värdena. Expansionshastigheterna beräknades till att vara signifikant högre än i litteraturen [4] för alla stjärnor utom Y Hya. De värden vi jämför med är dock baserad på data med lägre signal-brusförhållande och lägre osäkerhet i allmänhet [5] vilket är en indikation på att våra värden kan ha bättre säkerhet. Alla molekyler som hittades i frekvensspektrumet i Band 6 (215.4 - 217.4, 217.3-219.3, 230.2-231.2, 231.1-233.1 GHz) och Band 7 (330.3-331.3, 331.3-333.3, 342.5-344.5, 345.1-346.1 GHz), 15 totalt med 11 i kolrika stjärnor och 10 i syrerika stjärnor, var vanliga för sitt respektive slag. Undantaget var det nyligen (2016) upptäckta AIO [6], som detekterades i R Crt. Spektralindex,  $\alpha$ , beräknades från flödet i det kontinuerliga spektrumet för Band 6 (224.3-241.9 GHz) och band 7 (338.2-354.0 GHz). Temperaturen beräknades för stjärnorna med  $\alpha \approx 2$  (Y Hya och R Crt) och överensstämde med tidigare litterära värden [3, 4]. För stjärnorna med  $\alpha \neq 2$  (U Hya, R For och R Hya) beräknades stoftets massa,  $M_D$ , och stoftets massflödes hastighet,  $\dot{M}_D$ , med en antagen temperatur på  $T_{dust} = 100$  K. För uppmätt flöde 10% högre än förväntat (R For and R Hya), gavs värdena  $M_D = 10^{-5} M_{\odot}$  för båda stjärnorna, samt  $\dot{M}_D = 10^{-8} M_{\odot} yr^{-1}$  och  $\dot{M}_D = 10^{-7} M_{\odot} yr^{-1}$  för R For och R Hya respektive.

## Acknowledgements

We want to express our very great appreciation to our eminent supervisors Matthias Maercker and Elvire De Beck, who has guided us through the challenging waters of AGB stars in an excellent manner. Not only have they been patient with our endless stream of questions, but they have also taken their time to arrange a visit to the Onsala observatory.

Without the ALMA telescope, the DEATHSTAR project, its principal investigator Sofia Ramstedt and the data they have provided, this thesis would not have been possible. Therefore, we extend our greatest appreciation to everyone that has made the DEATHSTAR project and its substantial database a reality.

Furthermore, Sofia Ramstedt et al. 2008 [2] have developed an equation for estimating the gas mass-loss rates, which is central to our thesis. We refer to it only as of the Ramstedt equation even though we wish to credit everyone that contributed to its realisation.

We also want to offer our special thanks to Wouter Vlemmings, who held an inspiring lecture on interferometry, and who also gladly answered several questions on the same subject, which significantly improved our understanding.

Assistance provided by the staff of Chalmers Writing was much appreciated and did wonders of improving our writing. Without their help, the thesis would be far from what it is.

Our friends and fellow students Amanda Strömfors, Per Hirvonen, Sara Wäpling and Johan Gustafsson, who have done a similar thesis to ours deserve our utmost gratitude for the time they have generously taken to assist us with sources as well as taken part in discussions, which has resulted in the development of our thesis.

Finally, we wish to acknowledge the Department of Earth, Space and Environment of Chalmers University and especially our examiner Magnus Thomasson who has honoured us with the opportunity of doing this thesis with them.

Marcus Alm,  
Gabriel Angerd,  
Tomas Lundberg,  
Sebastian Oleszko,  
Alexander Wölfinger,  
*Gothenburg, May 2019*

# Contents

<b>1</b>	<b>Introduction</b>	<b>2</b>
1.1	Background . . . . .	2
1.2	Purpose . . . . .	3
1.3	Layout of the thesis . . . . .	3
<b>2</b>	<b>Stars on the Asymptotic Giant Branch</b>	<b>4</b>
2.1	Hertzsprung–Russell diagram . . . . .	4
2.2	Evolution . . . . .	4
2.3	Structure and general properties . . . . .	5
2.4	Circumstellar envelope . . . . .	7
2.4.1	The standard CSE model . . . . .	7
2.4.2	Molecular gas . . . . .	7
2.4.3	Dust . . . . .	8
2.4.4	Wind driving mechanism . . . . .	8
2.4.4.1	Pulsations . . . . .	9
2.4.4.2	Dust driven outflow . . . . .	9
2.5	Mass-loss rate . . . . .	10
<b>3</b>	<b>Methods for Analysing AGB Stars</b>	<b>11</b>
3.1	Interferometry . . . . .	11
3.2	Distance measurements . . . . .	12
3.3	Spectroscopy . . . . .	13
3.4	Radiative transfer . . . . .	13
3.5	Sub-mm wave observations of AGB stars . . . . .	14
3.5.1	Analysis of emission lines . . . . .	14
3.5.2	Analysis of continuum emission . . . . .	16
<b>4</b>	<b>Observations and Data Analysis</b>	<b>19</b>
4.1	The sample of stars . . . . .	19
4.2	Observations . . . . .	19
4.3	Information gathering . . . . .	20
4.4	Data analysis . . . . .	20
4.4.1	Integrated flux density . . . . .	21
4.4.2	Emission lines . . . . .	22
4.4.2.1	Gas mass-loss rate . . . . .	22
4.4.2.2	Molecular identification . . . . .	22

4.4.3	Continuum emission . . . . .	23
<b>5</b>	<b>Results</b>	<b>24</b>
5.1	Emission lines . . . . .	24
5.1.1	Mass loss-rate . . . . .	24
5.1.2	Molecular catalogue . . . . .	25
5.2	Continuum emission - dust . . . . .	28
<b>6</b>	<b>Discussion and Conclusions</b>	<b>33</b>
6.1	Gas mass-loss rate . . . . .	33
6.1.1	Distance measurement - $D$ . . . . .	33
6.1.2	CO-line intensity - $I_{CO}$ . . . . .	34
6.1.3	Beam size - $\Theta_b$ . . . . .	34
6.1.4	Expansion velocity - $v_{exp}$ . . . . .	34
6.1.5	Obtained gas mass-loss rates . . . . .	35
6.2	Identified Molecules in the CSEs . . . . .	36
6.3	Continuum emission - dust . . . . .	38
6.4	Closing remarks . . . . .	39
	<b>Bibliography</b>	<b>39</b>
<b>A</b>	<b>Acronyms</b>	<b>II</b>
<b>B</b>	<b>Figures</b>	<b>III</b>
B.1	Emission Lines . . . . .	III

# 1

## Introduction

Stars with an initial mass from about one half to eight solar masses ( $M_{\odot}$ ), in their late stage of evolution, become stars on the *asymptotic giant branch* (AGB)[7]. In this stage, the stars spend just a small fraction of their lives, but even so, this is when some of their most life-changing events occur. During the AGB-phase the stars begin to lose mass on the order of  $10^{-8} - 10^{-5}M_{\odot}$  per year[8]. This matter eventually gets mixed up with the *interstellar medium* (ISM) upon which it contributes to the gas and dust clouds from which new stars and planets are born.

Inside AGB stars, due to their convective interior and abundance of different elements, a process which produces elements heavier than iron can occur. Something otherwise only achieved by supernovae or merging neutron stars. In fact, half of the elements heavier than iron are created in AGB stars and are spread out in the galaxy through their mass-loss mechanisms[9]. Therefore, knowing more about the stars that create a considerable share of the fundamental building blocks which constitutes our universe is a clear motivation for studying AGB stars. This knowledge will further our understanding of the evolution of our galaxy, the history of our solar system and perhaps even of where and how life begins.

### 1.1 Background

One of the most important features for studying AGB stars is its *circumstellar envelope* (CSE). The CSE is the area outside of the star's atmosphere, which reaches up to 10000 stellar radii from the star. Here a steady outflow of mass occurs at speeds in the order of  $10 \text{ km s}^{-1}$ . The envelope gives us information about what processes are present inside the star, what composition it has and what types of, and how much material is spread out to the ISM. The envelope can also give us an overview of the history of the star from the moment it started ejecting mass.

*The Atacama Compact Array* (ACA) which is a part of the *Atacama Large Millimeter/submillimeter Array* (ALMA) in Chile has been used in the DEATHSTAR (DEtermining Accurate mass-loss rates of THERmally pulsing AGB STARS) project[1] to observe around 80 stars in our solar neighbourhood (within 1 kpc). DEATHSTAR provides the data for this thesis, which constitutes several frequency spectra in Band 6 (211-275 GHz) and Band 7 (275-373 GHz). From these frequency spectra the detection of various molecules can be made due to their rotational transitions. By analysing the distribution and intensity of these molecular transitions in the envelope and applying existing equations, we can also establish mass-loss rate estimates of the stars. The mass-loss rate is the most important driver in the evolution of an AGB star and hence has a high scientific value[8, 2].

It is not only gas molecules we can analyse from the frequency spectra, but also another

component of the envelopes, stellar dust. The dust plays a crucial role in accelerating the gas in the envelopes by absorbing radiation from the star and dragging the gas along, thus enabling the mass-loss[7]. Contrary to the gas molecules in the CSE, whose spectral lines we often have precise knowledge of, the dust grains are large and complex, and hence there are no known transitions which we can observe. Therefore, in the case of the dust, we must analyse the black-body radiation in continuum frequency spans. From the continuum measurements at a given wavelength, we can apply known equations to conclude the amount and distribution of the stellar dust.

## 1.2 Purpose

This thesis aims to perform an analysis of the AGB stars Y Hya, U Hya, R For, R Hya and R Crt with data from the DEATHSTAR project [1]. The analysis will consist of three major areas. From the spectral lines in the data, we will identify what molecules are present in the CSEs of the different stars. Furthermore, the specific rotational transitions of CO,  $J = 2 \rightarrow 1$  and  $J = 3 \rightarrow 2$ , will be used to estimate the gas mass-loss rates with a formula (Equation (3.8)) based on radiative transfer modelling[2]. The accuracy of this estimate will be examined with error analysis and the comparison to existing values in the literature. Continuum emission spectra will be used to calculate the spectral index, the temperature of the star and ultimately, if dust seems to be present, the dust mass-loss rate. We limit this thesis to the study of only five stars in the solar neighbourhood using data from one source in a limited frequency range (Band 6 and Band 7 of ALMA). Also, due to the lack of time, we disregard of analysing the possible observational or data inadequacies resulting from weather conditions, filters, calibrations and other specifications etc.

## 1.3 Layout of the thesis

In Chapter 2 we introduce AGB stars. In Chapter 3, methods useful for analysing AGB stars are presented. Observations and data reduction is covered in Chapter 4. After that, our results are presented in Chapter 5 and we make our conclusions and final remarks in Chapter 6. We also present a list of acronyms in Appendix A, which can be useful for the reader as a reference. In Appendix B, figures that did not fit in Chapter 5 are shown.

# 2

## Stars on the Asymptotic Giant Branch

The life-span of a star is predominately determined by its mass. The stellar-group with masses between  $0.5 - 8M_{\odot}$  (solar masses) takes a certain evolutionary path towards termination. These stars are in their final stages classified by belonging to the *Asymptotic Giant Branch* (AGB), and are generally referred to as AGB stars [7].

### 2.1 Hertzsprung–Russell diagram

In Figure 2.1 stars' temperature are plotted against luminosity. This is a *Hertzsprung-Russell diagram* (HR-diagram), in which we can see the relations amongst fundamental stellar quantities: luminosity  $L$ , temperature  $T$ , mass  $M$ , radius  $R$  and lifetime  $\tau$ [10]. We see that the bulk of the stars are along a somewhat straight line, which roughly corresponds to  $L \propto T^6$ . These are the so-called *main sequence stars*.

A star is not stationary in its location in the HR-diagram during its lifetime. Thus, when the evolution of a star is discussed, it is useful to express the different phases in terms of movement in the HR-diagram to understand how the relations amongst the stellar quantities are changed. Some significant alternations of the basic stellar relations occur in late-life evolution why there are stars deviating from the  $T^6$  line. It is common to use the *zero age main sequence* (ZAMS) as a starting point for where the star begins its life.

### 2.2 Evolution

A  $0.5 - 8M_{\odot}$  star spends billions of years after its creation on the main sequence burning<sup>1</sup> hydrogen in its core. When hydrogen in the core eventually is depleted, the star will begin to change rapidly. The equilibrium between radiation pressure, generated by fusion, and gravity will break upon hydrogen depletion since the radiation pressure depends on the nucleosynthesis of hydrogen to helium. This imbalance will initiate the first movements up the red giant branch (RGB) in the HR-diagram, Figure 2.2, and the star will swell up to several hundred times its original size[8]. Hydrogen will continue to burn in a shell surrounding the growing helium core. Eventually, the pressure and temperature will be high enough, and helium in the core will ignite. This happens at the peak of the RGB in Figure 2.2 and causes to star to move to the horizontal branch where the temperature steadily increases while the luminosity somewhat decreases. After about one hundred million years the star will

---

<sup>1</sup>Burning as in the process of fusion.

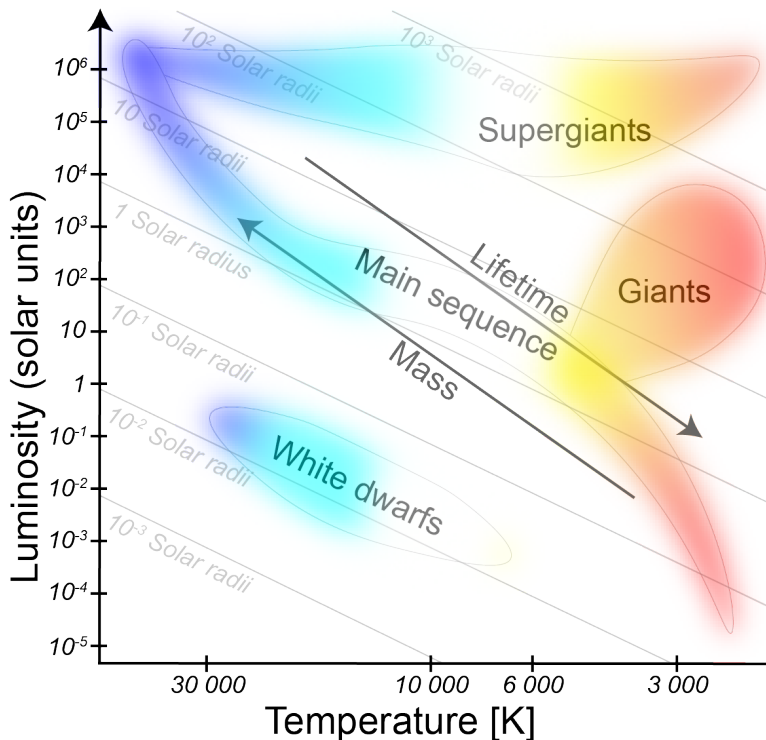


**Figure 2.1:** Schematic drawing of an HR diagram. On the left axis there is a logarithmic scale of luminosity in  $L_{\odot}$  and on the bottom axis a logarithmic scale of temperature in K increasing to the left. Diagonal lines in the diagram indicate different stellar radii in  $R_{\odot}$ . The line going from the top left corner to the bottom right corner is called the main sequence and corresponds approximately to  $L \propto T^6$ . Along the main sequence mass increases from about  $0.1M_{\odot}$  to  $100M_{\odot}$  while lifetime increases in the opposite direction. The relations  $L \propto M^3$ ,  $T \propto M/R$  and  $\tau \propto M^{-2}$  can all be read from the HR-diagram. The lifetime relation  $\tau \propto M^{-2}$  is only relevant for stars on the main sequence.

stop burning helium in the core, leave the horizontal branch and begin its second ascent up the giant branch, specifically the Asymptotic giant branch. During the AGB-phase, several processes occur. One of these, which we will explore further in this thesis, is the fact that a star on the AGB begins to lose mass. Instabilities due to this mass-loss in combination with further depletion of fusionable material finally causes the star to leave the AGB by ejecting its outer hydrogen envelope. The ejection transforms the star into a planetary nebula, and it will eventually settle in the HR-diagram as a white dwarf, Figure 2.2.

## 2.3 Structure and general properties

At the onset of the AGB phase, the star consists of an inert carbon and oxygen core encompassed by thin shells: an inner shell of burning helium and a shell of burning hydrogen outside of it. Burning of the two shells is the primary driving force to sustain the star during the AGB, and the core is only held up by its electron-degeneracy pressure. Outside the two shells lies a convective envelope, extending to the surface of the star. However, the surface

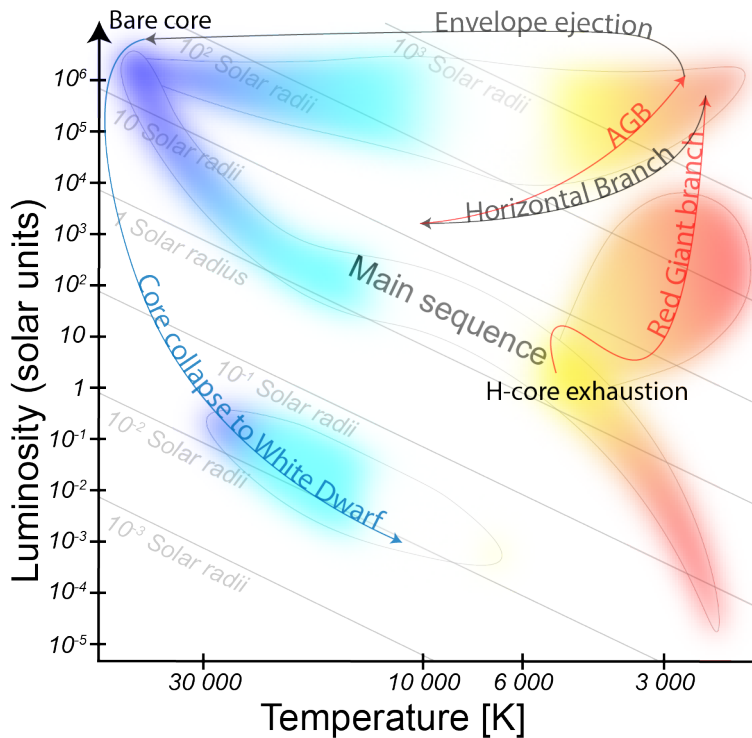


**Figure 2.2:** A Schematic evolutionary path of a star with mass  $0.5 - 8M_{\odot}$ . See text for details.

and boundaries of the star is a loosely defined limit since the convective envelope blends together with the star's atmosphere. The mass distribution of the star is very different from the structural and spatial distribution. Figure 2.3 shows the difference in the proportion of mass to volume, displaying the substantial differences in the density of the regions. For a  $1M_{\odot}$  AGB star approximately 50% of the mass lies within 2% of the radius [7]. This is in significant contrast to a main sequence star which has a smoother density distribution.

In Figure 2.4, a schematic cross-section of an AGB star is shown. The interior of an AGB star is an oxygen and carbon-rich environment. Convective flows in the stellar interior intersperse the elements and help fuel the inner burning shells with more hydrogen. Newly formed carbon enrich the outer parts of the star as it evolves and changes the ratio of C/O. The C/O-ratio determines the spectral type of the AGB star. Spectral types vary from M-stars ( $C/O \approx 0.5$ ) to C-stars or carbon stars ( $C/O > 1$ ). There are however limitations to which stars can reach a C/O-ratio of a carbon star; the initial mass needs to be  $1.5 - 4 M_{\odot}$  [7]. The longer a star spends on the AGB, the more carbon gets mixed up to the surface through the convective interior.

Typical stellar quantities for an AGB star is a surface temperature of about 3000 K and a luminosity in the magnitude of  $10^3 - 10^4 L_{\odot}$ , which implies that the star has a radius of a couple of hundred solar radii [7].

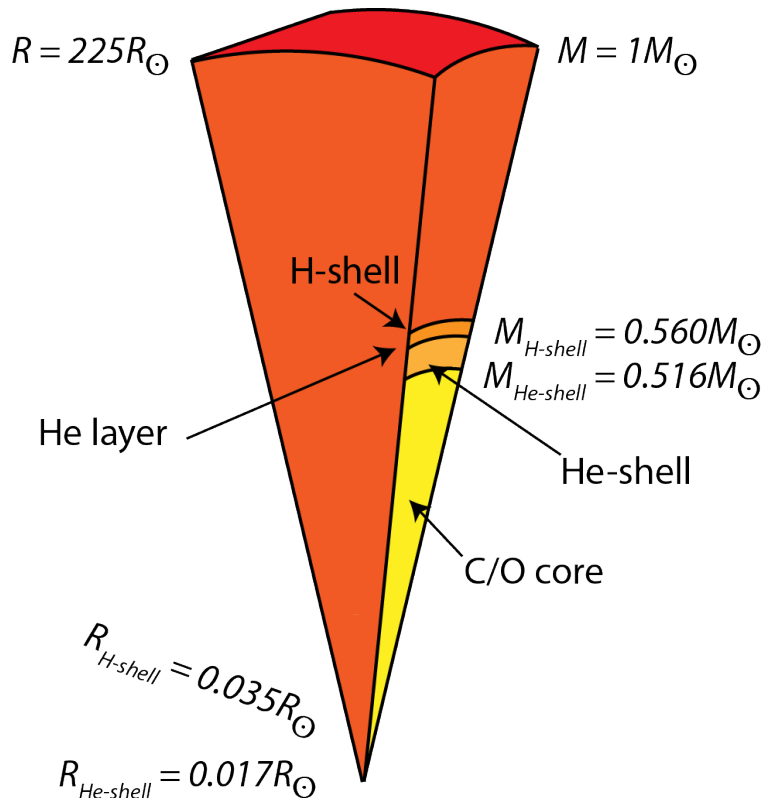


**Figure 2.3:** Schematic view of the structure of a  $1M_{\odot}$  AGB star. To the *right*, regions are plotted against mass fraction while they on the *left* side are plotted against radius. Adapted from [11]

## 2.4 Circumstellar envelope

Material discharged from the stellar atmosphere gradually builds up a *Circumstellar envelope* (CSE), see Figure 2.4. The CSE functions as an observational tool for studying AGB stars and provides information on the evolution of the star, its ongoing internal processes and the mass-loss process. In this section, we will cover how a CSE is structured, its main constituents, namely molecular gas and dust, and finally the mechanism with which it forms.

### 2.4.1 The standard CSE model

The *standard CSE model* is constructed from assumptions which in theory would hold over long time scales. The primary driving forces on the gas and dust in the stellar wind can be assumed to be governed by radiation pressure and gravity. Therefore, a spherically symmetrical mass-flow can be assumed [7]. The velocity profile of the mass-flow can be considered constant (usually this is true at large radii), radially dependent or determined through dynamical models.

### 2.4.2 Molecular gas

The chemical composition of matter in the stellar atmosphere is a determining factor of what to expect in the CSE. A significant factor to what molecules will form in the atmosphere is the C/O-ratio of the star. The high binding energy of the CO-molecule causes the less

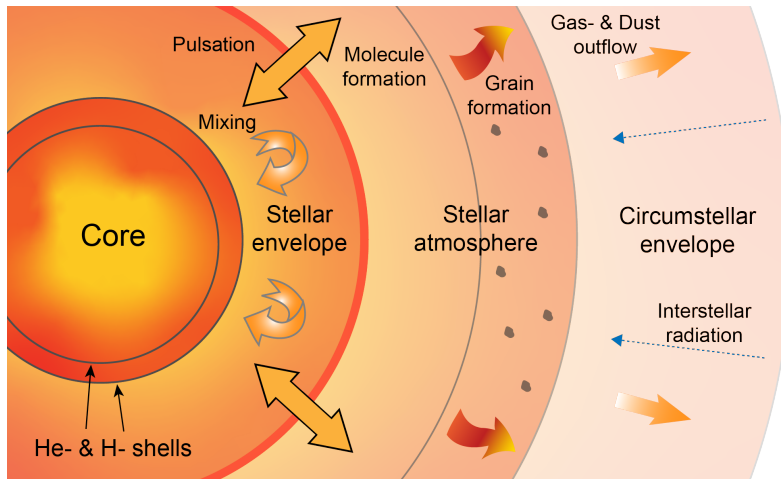


**Figure 2.4:** Schematic view of the processes taking place in, and outside of, an AGB star. Beyond the inert C/O-core lies a He- and H-shell where fusion takes place. In the convective stellar envelope mixing of elements occurs while it also propagates pulsations instigated from the interiors. In the stellar atmosphere, molecules are formed closer to the star, and further out, where the temperatures are lower, dust grains are condensed. The dust grains drive the surrounding molecular gas and create an outflow into the circumstellar envelope. Interstellar radiation causes disassociation of some molecules in the CSE. Adapted from [12]

abundant of the two elements to become mostly bound up in CO. Consequently, a star with a higher abundance of carbon (C-type) usually has more carbon-based molecules such as, CN, C<sub>2</sub>, C<sub>2</sub>H<sub>2</sub>, HCN while oxygen-rich (M-type) stars produce more H<sub>2</sub>O, TiO, VO, SiO [7]. Around one hundred different molecules have been detected in the CSEs of AGB stars [8]. Two molecules that are always expected in large amounts are H<sub>2</sub> and CO.

### 2.4.3 Dust

In comparison to gas, dust is a much rarer building block of the CSE, and the gas to dust mass-ratio can usually be expected as 1:100 [2]. Depending on what molecules are present in the CSE, different dust species with different properties will be created. The present dust precursor molecules, called monomers, can in the right conditions combine and form larger polymers. When the polymers become large enough to act as a solid, typically 0.1 – 1 μm [13], we call them dust grains [8]. For dust to condense the temperature needs to be sufficiently low. This critical point is called the condensation temperature,  $T_c$ , and is commonly between 1000 K and 1500 K depending on the species of dust [13]. Where the condensation takes place depends on the temperature of the star and the distance from it. The position of condensation, typically a few stellar radii from the surface of the star, plays a central role in the mass-loss mechanism which will become apparent in the following sections.

### 2.4.4 Wind driving mechanism

For a CSE to form, some mechanism is required to trigger and maintain an outflow of mass. The consensus in the astronomy community is that the outflow is caused by mainly

two effects: pulsations<sup>2</sup> in the star which levitates material, and dust, which propelled by radiation pressure drags the gas along with it [13]. The basics of the wind driving mechanism, the pulsations, grain formation and the resulting outflow can be seen in Figure 2.4.

#### 2.4.4.1 Pulsations

Pulsations in the interiors of AGB stars arise because of disturbances in the hydrostatic equilibrium between the radiation pressure and gravity. These perturbations cause oscillations in the outward directed energy, which transfers into sound waves. In most stars, the pulsations would not propagate to the outer regions and would instead die out due to the inverse quadratic scaling of spherical expansion. However, since AGB stars, in comparison to other stars, have a significant fraction of their mass within a small radius around the core, their density profiles are very steep, which can be seen in Figure 2.3. Therefore, the pulsations do not die out, but instead, both the amplitude and velocity of the pulsations increase.

Another effect of the lower density is a decreased speed of sound. As the waves increase in speed and amplitude, they eventually equal the speed of sound, creating a supersonic shock. In combination with the fact that the matter at the surface of the AGB stars is loosely bound by gravity due to its large radius, the shock can cause shells of mass to be thrown out into the stellar atmosphere. However, the pulsations are not quite powerful enough for the shells to overcome gravity and entirely escape the star; instead, they eventually fall back to the surface. Some additional process is needed to drive the stellar wind that causes the mass-loss.

#### 2.4.4.2 Dust driven outflow

The dust grains which are formed a few stellar radii from the surface of its star are huge in comparison to the surrounding gas in the CSE. Some species of dust are also prone to absorb radiation in the infrared range, which happens to be where the peak of AGB star black-body spectra lies. These two facts, i.e. the size and absorption properties of the dust, together with the pulsations, lead to the solution of the most accepted theory of the wind driving mechanism for AGB stars, namely the *Pulsation enhanced dust driven outflow* (PEDDRO)[7].

If the shock waves are powerful enough to lift some mass to the radius of condensation, the dust can take over and drive the outflow. It does this by being accelerated due to radiation pressure from the infrared light that originates from the star. The gas molecules in the CSE are all too small to be accelerated in the same manner. Instead, the dust grains drag the gas along while it propagates through the CSE by transferring momentum through collisions. The resulting outcome is an outflow of mass, consisting of both gas and dust. Once the gas and dust has passed a specific accelerating zone, about  $10R_*$  from the surface [7], and reached escape velocity, it continues to spread out in a constant speed.

The PEDDRO scenario causes bounds on the mass-loss rate,  $\dot{M}$ . Since light from the star propels the dust grains, the acceleration depends significantly on the radiation intensity. If the CSE is thick, that is if the mass-loss rate is large, the optical depth,  $\tau$ , explained in

---

<sup>2</sup>These pulsations are not to be confused with the thermal pulses of AGB stars that are of entirely different nature and time scales. The periods for the pulsations of which we discuss here are in the order of 100 to 1000 days while the thermal pulses are  $10^4$  to  $10^5$  years[7].

Section 3.4, increases. A greater optical depth, in turn, causes a decrease in the intensity, resulting in less radiation pressure on the dust grains. For a critical  $\dot{M}$ , the intensity is too small to drive the acceleration of the dust and outflow is unattainable. In contrast, if the mass-loss rate is small, dust collisions with gas become less probable. Therefore, at a critical  $\dot{M}$  where dust has a too small drag effect on the gas, a steady outflow is, again, not possible. Calculations on these two effects give a range of possible mass-loss rates to  $10^{-7} - 10^{-5} M_{\odot}$  per year[8]. These bounds are in approximate agreement with observations, which is a reason to believe that the PEDDRO scenario is likely to be the main wind driving mechanism of AGB stars[7].

## 2.5 Mass-loss rate

The mass-loss rate,  $\dot{M}$ , is the single most important characteristic of an AGB star[8, 2]. It is the main driver of evolution in the final stages of low- and intermediate-mass stars. The mass of a star is, as mentioned at the beginning of the chapter, a major predictor of the lifetime of a star and also of its maximum size and luminosity. Naturally, the mass-loss, therefore, affects these quantities[14]. AGB stars also play an integral part in providing mass to the ISM as well as contributing to the overall luminosity in intermediate-age stellar systems. Therefore, to establish a precise estimate of the mass-loss rate is important for studying extragalactic stellar populations and how they affect the evolution of the galaxy.

Accurate mass-loss rate estimators are however challenging to develop due to the large number of stellar properties and processes that affect  $\dot{M}$ : temperature, luminosity, metallicity and chemistry, wind properties, pulsations, mass and temporal variations to name a few[7]. Nonetheless, the importance of development in the area is essential since an error on the mass-loss rate of just a factor two has a significant effect on the evolution of the star, its nucleosynthesis and the rate of which the star provides mass to the ISM[2]. In Section 3.5, we will present methods for estimating both the gas and dust mass-loss rate.

# 3

## Methods for Analysing AGB Stars

In this chapter we begin by describing the observational method of interferometry. We also discuss the theory behind two different methods for analysing the electromagnetic radiation received from a source: spectroscopy and radiative transfer. Finally, we present models and equations specific for AGB star observations in the sub-mm range, which is the type of observations we use in this thesis.

### 3.1 Interferometry

The resolution of a telescope is proportional to the observed electromagnetic wavelength,  $\lambda$ , and the diameter of the reflective dish,  $D$ , according to

$$\Delta\theta \propto \frac{\lambda}{D}. \quad (3.1)$$

For sub-mm wavelengths, which is relevant when observing AGB-stars and their CSE's, a single dish telescope is not viable for high resolution. The use of interferometry can be implemented to solve this problem. Instead of only using one dish, interferometry makes use of several different dishes, combining their observations and consequently achieves an effective diameter equal to the longest distance between any two telescopes.

Interferometry is based on the *Van Cittert-Zernike theorem* [15, 16] which states that under certain conditions<sup>1</sup>, the inverse Fourier transform of the spatial coherence function, also called the visibility function, is the intensity distribution of the incoming radiation for a given wavelength  $\lambda$  i.e. the picture we want of the source. This relation is explicitly written as

$$I(x, y) = \mathcal{F}^{-1}\left[V\left(\frac{u}{\lambda}, \frac{v}{\lambda}\right)\right], \quad (3.2)$$

where  $x$  and  $y$  are the sky coordinates and  $u$  and  $v$  the coordinates of the relative position of two telescopes projected in the plane orthogonal to the source, called the baseline vector. The visibility function is, in the case of astronomical interferometry, approximated by correlating the signals of different telescopes. For the correlation, the plane waves that arrive at the telescopes at different times have to be matched with accuracy proportional to the wavelength, see Figure 3.1.

The sample obtained for the visibility function depends on the baselines; what length they have and their orientation relative to the source. With  $N$  telescopes,  $N(N - 1)/2$  baselines are attained. If the telescopes are positioned such that they create a varied distribution of different baselines the result will be a good approximation of the visibility function. If one

---

<sup>1</sup>We assume that these conditions are satisfied for the cases we touch without going into any details.

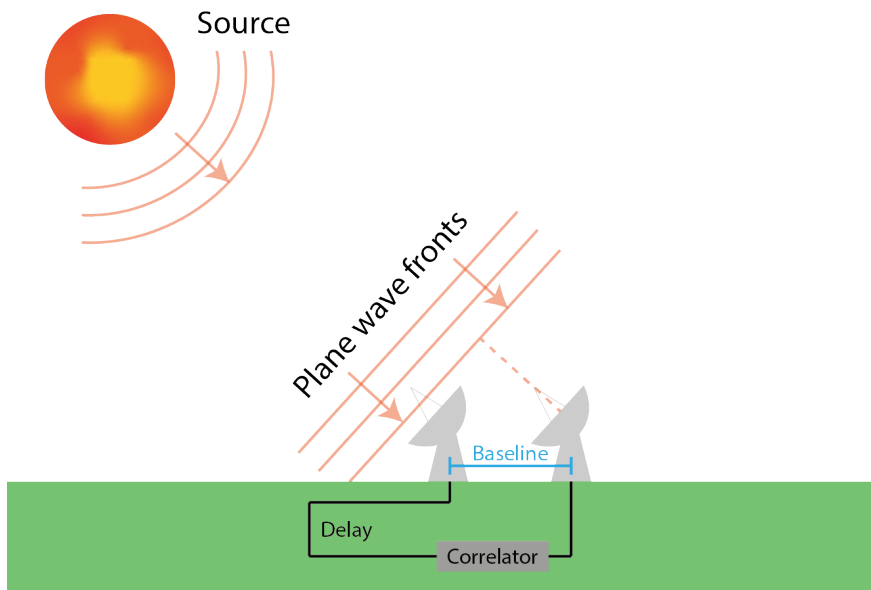


**Figure 3.1:** Basic concepts of interferometry. The plane waves of a distance source reach the two telescopes at different times. A delay is added before the signals can be correlated.

observes during a period which allows the Earth to rotate, the baselines are also changing their orientation with regards to the source. The changing baselines effectively create many more pairs of telescopes and thus a much better approximation of the visibility function is achieved.

## 3.2 Distance measurements

An important parameter in many astronomical calculations is distance. It is difficult to determine and is often a source of significant uncertainty. In this thesis, we make use of two different distance estimators: The *parallax method* and a *period-luminosity relation* (P-L). Even if there are other more accurate ways to obtain the distance to an AGB star, those methods cannot always be implemented[17].

The parallax method uses the angle (called the parallax) created by observing an object on one side of our orbit and then once more on the other side (six months later). The two observations are then compared to the background to create the parallax and thus obtaining its distance. However, the parallax method does not work well for large objects. AGB stars typically have a radius of several au making the object constructing the parallax larger than the orbit of Earth as seen in Figure 3.2. This creates problems[17]. When measuring the location of a star to the background, it is the brightest spot on the star that defines its position. The brightest spot is not constant why different measurements derive different distances.

The (P-L) relation uses known periodic luminosity fluctuations. Specific periods relate to certain luminosities why measurement of the period of the star can infer its luminosity and therefore, together with the brightness, its distance.

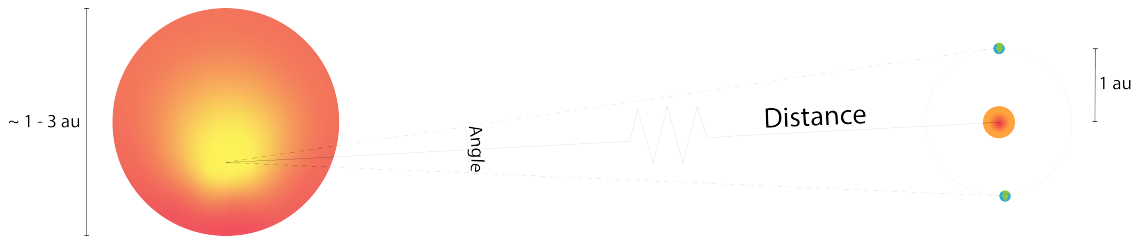


**Figure 3.2:** Illustration of the parallax method distance measurement of an AGB star. Also shown, is the problem with the size of the AGB star and the possible variation of the bright spot.

### 3.3 Spectroscopy

The study of molecular spectroscopy is essential for understanding the methods of this thesis. Having a molecule with two or more atoms creates new ways to emit light, enabling what's called rotational and vibrational transitions. The combinations of the emitted light from these transitions create a fingerprint for each molecule which we can use to identify them in a frequency spectrum. The energy levels of a linear molecule under the rigid motor model are given by

$$E = BJ(J + 1), \quad B = \frac{h}{8\pi cI}, \quad (3.3)$$

where  $J$  is the rotational quantum number,  $B$  the rotational constant, which contains the moment of inertia  $I$ , Planck's constant  $h$  and the speed of light  $c$ .

A phenomenon common in the observation of emission lines from stars is *Microwave Amplification by Stimulated Emission of Radiation* (maser). Masers occur when a photon interacts with an excited molecule, leading to the emission of a photon with similar direction, frequency and phase. This can lead to distinctly increased intensities at certain frequencies in a spectrum, which in turn can cause certain emission lines to have unexpected profiles.

Another aspect of spectroscopy is the black-body radiation given by

$$B_\nu(\nu, T) = \frac{2h\nu^3}{c^2} \frac{1}{e^{\frac{h\nu}{k_B T}} - 1}, \quad (3.4)$$

where  $k_B$  Boltzmann's constant,  $T$  temperature and  $\nu$  frequency. An approximation can easily be applied to this expression if the condition  $h\nu \ll k_B T$  holds. When this argument is satisfied, we obtain the Rayleigh-Jeans approximation

$$B_\nu(\nu, T) = \frac{2\nu^2}{c^2} k_B T. \quad (3.5)$$

### 3.4 Radiative transfer

Radiative transfer describes how electromagnetic waves transfer through various mediums. One parameter of radiative transfer is the optical depth  $\tau$ , which describes how much electromagnetic radiation is permeated through a medium as seen in figure 3.3. The equation of optical depth is given by

$$\tau_\nu = a_\nu \int_{r_e}^{r_i} \rho_d(r) dr, \quad (3.6)$$

where  $a_{nu}$  is the absorption coefficient of the medium and  $\rho_d(r)$  the mass density distribution of the medium.  $\tau$  ultimately leads to information about the medium obstructing the source. One can make calculations of how molecular lines will look after being affected by a medium by using the equation of radiative transfer

$$dI_\nu = -I_\nu d\tau_\nu + S_\nu d\tau_\nu, \quad S_\nu = \frac{j_\nu}{a_\nu}, \quad (3.7)$$

where  $S_\nu$  is the source function that characterises the medium's rate of absorbing and reemitting photons, with  $j_\nu$  as the emission coefficient.

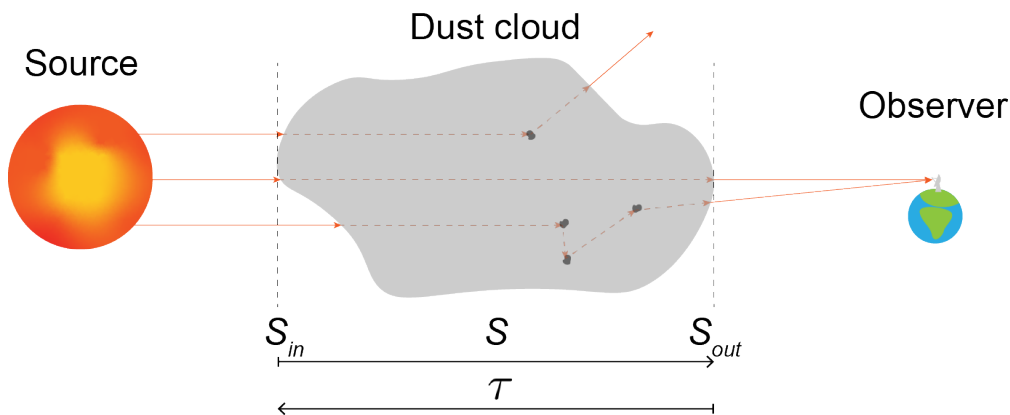


**Figure 3.3:** Light from the source is emitted towards the location of the observer. Between the source and the observer is a dust cloud with the optical depth  $\tau_\nu$ . Altering the properties of the source light according to Equation (3.7).

## 3.5 Sub-mm wave observations of AGB stars

We now present AGB specific methods and equations for sub-mm observations in the 211-373 GHz range (Band 6 and Band 7 of ALMA) primarily based on spectroscopy and radiative transfer. We split the data into two different classes. In the first, a broader frequency interval is divided into several frequency bins, usually with a width of a few hundred kHz. This means that our frequency resolution also is a few hundred kHz why we can identify spectral lines from molecules in the CSE. In the second, all emission in a frequency interval of about 10 GHz is gathered in a single picture. Consequently, we achieve a much lower resolution but can instead cover a wider range at once, which is useful when analysing black-body radiation.

### 3.5.1 Analysis of emission lines

With a high-frequency resolution, we can identify specific molecules through their rotational transitions. CO is, after molecular hydrogen, the most common molecule in the CSE[7] and is usually present in the entire CSE. Therefore, it is a good start to look at a transition of CO. We can get an overview of the morphology of the CSE, the expansion velocity of the gas and the radial velocity of the star relative to the sun. If the CSE is emitting radiation from a specific CO-transition, we can relate our data of frequency bins,  $\nu$ , to the known rest frequency,  $\nu_0$ , of the transition through Doppler shift. We can then see how fast the emitting

region must travel with regards to Earth for the received frequency to shift to  $\nu_0$  as

$$v = \frac{\nu_0 - \nu}{\nu_0} c.$$

In Figure 3.4a we can observe an example of a broadened CO emission line from an AGB star where Equation (3.5.1) have been used. Here  $v = 0$  corresponds to the transition frequency  $\nu_0$ . Since the line is not centred around 0, and if we assume a spherical homogenous outflow, the star must be travelling towards us with  $v_{star}$  to cause the shift from  $\nu_0$ .

The width of the emission line tells us how fast the gas is expanding from the star. The regions closest and furthest away from us will have their velocity in our radial direction, as seen in Figure 3.4b. Therefore, we can add these extreme values to  $\Delta v$  and divide by 2 to get the expansion velocity as  $v_{exp} = \Delta v/2$ .

The flatness of the line in Figure 3.4a can be explained with the fact that we see all radial velocity components exactly twice, once from each half of the CSE, Figure 3.4b. This is true for all radial cross-sections except those that provide us with the extreme values, whose radial components we only see once. Line profiles that deviate from this flat-top profile, which can be seen in Figure 5.2, can be due to optical thick lines ( $^{13}\text{CO}$  for example), masers or that the beam does not cover the entire CSE etc.

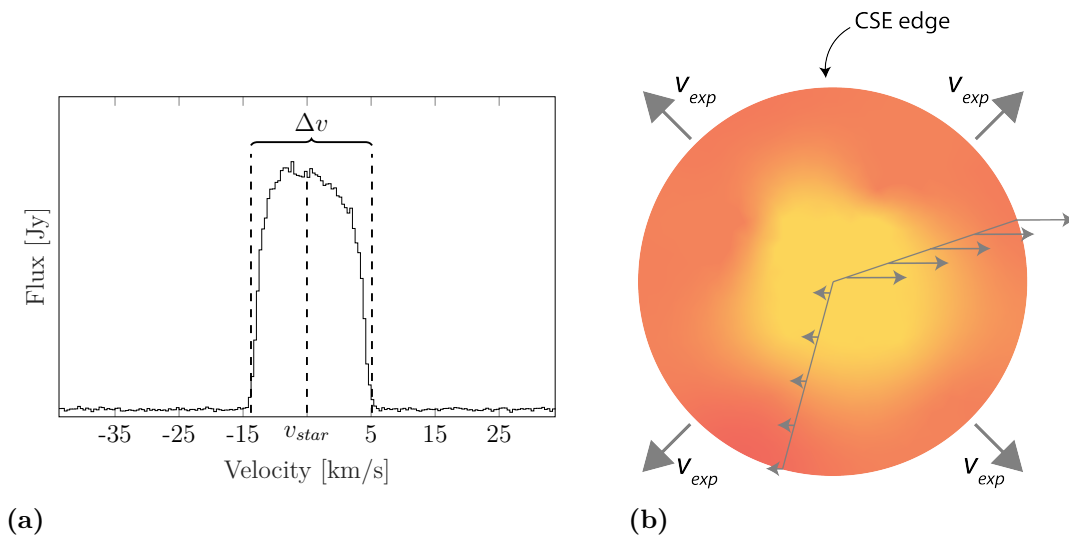


**Figure 3.4:** (a): Emission line from where we can read  $v_{star}$  and  $\Delta v$  which gives us the expansion velocity  $v_{exp} = \Delta v/2$ . (b): Spherical symmetric CSE with constant expansion velocity in all directions. If Earth is positioned to the *left* of the CSE in the figure, the *right* regions of the CSE corresponds to emission on the right side of the line in (a) and vice versa. The vertical arrows in (b) are the radial velocity components of different cross sections.

Except for giving us information on the velocity of the star and its gas, as well as the structure of the CSE, the emission lines can be used to estimate the important mass-loss rate discussed in Section 2.5. An equation for the mass-loss rate is presented in Appendix A of Ramstedt et al. 2008 [2]. The equation makes use of CO rotational emission lines and is based on radiative transfer modelling.

With an estimate of the CO to  $\text{H}_2$  ratio,  $f_{CO}$ , the distance to the star in kpc  $D$ , the beam size of the used telescope in arc seconds  $\Theta_B$ , the integrated intensity of the observed CO line

$I_{CO}$  in  $\text{K km s}^{-1}$  (kelvin kilometres per second) and the measured expansion velocity  $v_{exp}$ , the mass-loss rate can be expressed in solar masses per year as

$$\dot{M} = s_j \left( I_{CO} \Theta_b^2 D^2 \right)^{a_j} v_{exp}^{b_j} f_{CO}^{-c_j}, \quad (3.8)$$

where  $s_j$ ,  $a_j$ ,  $b_j$  and  $c_j$  are transition specific constants found in Table 3.1.

**Table 3.1:** Constants and exponents for the CO rotational transitions in Band 6 and Band 7 relevant for Equation (3.8)[2].

Transition	$s_J$	$a_J$	$b_J$	$c_J$
$J = 2 \rightarrow 1$	$1.3(\pm 0.7) \cdot 10^{-11}$	$0.82(\pm 0.03)$	$0.46(\pm 0.13)$	$0.59(\pm 0.07)$
$J = 3 \rightarrow 2$	$3.8(\pm 3.4) \cdot 10^{-11}$	$0.91(\pm 0.04)$	$0.39(\pm 0.13)$	$0.45(\pm 0.07)$

Finally, the emission lines can be used to make a catalogue of the present molecules in the CSE. As mentioned in Section 2.4.2, just under one hundred different molecules have been detected in the CSEs of AGB stars. For these molecules, there are tens of thousands of registered transitions only in Band 6 and Band 7[18]. One must therefore be careful not to mislabel while classifying molecules. However, many of the molecules have several different transitions in Band 6 and Band 7. CO, for example, has a transition in Band 6 at 230.5 GHz ( $J = 2 \rightarrow 1$ ) and one in Band 7 at 348.8 GHz ( $J = 3 \rightarrow 2$ ). If several or all the transitions are detected, a greater certainty can be established.

### 3.5.2 Analysis of continuum emission

The emissions we analyse from the continuum originates from black-body radiation. The star radiates light from its surface as a black-body and the bulk of the intensity we receive typically emanates directly from the star. The dust in the CSE is a good absorber of light in the IR-range, which is why some fraction of the starlight is absorbed and re-emitted in a lower frequency related to the dust temperature. That is, the dust also (re-)emits as a black-body. In Figure 3.5 we see an example with a black-body spectrum of a star with a temperature of 2000 K and dust with 700 K. If you add both spectra the *spectral emission distribution* (SED) will deviate from a black-body.

Since we are observing relative low frequencies,  $h\nu \ll k_B T$  is satisfied, and we can use the Rayleigh-Jeans approximation, Equation (3.5), and state that the specific intensity for a black-body  $I_\nu \propto \nu^2$ . Thus, we can calculate the *spectral index*,  $\alpha$ , which indicate the slope of the black-body curve,  $I_\nu \propto \nu^\alpha$ , as

$$\alpha = \frac{\log I_7 - \log I_6}{\log \nu_7 - \log \nu_6} = \frac{\log I_7/I_6}{\log \nu_7/\nu_6}, \quad (3.9)$$

where  $I_6$  and  $I_7$  are the intensities from Band 6 and Band 7 corresponding to the central frequencies,  $\nu_6$  and  $\nu_7$ . For a pure black-body spectrum we expect  $\alpha = 2$ . If dust is present, as in Figure 3.5, the slope can vary over the SED and  $\alpha$  is therefore not necessarily equal to two.

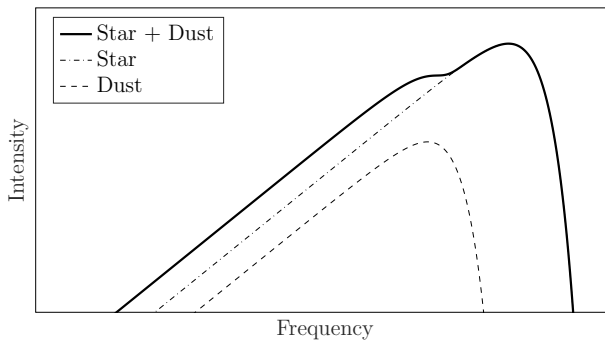


**Figure 3.5:** The black-body spectra of a star with 2500 K (*dash-dot line*) and of dust with 100 K (*dashed line*) as well as their added SED (*solid line*), all plotted in log-log. The  $x$ -axis indicate frequency and the  $y$ -axis intensity, both in arbitrary units. The black-body spectrum of the dust has been weighted by a factor of 500 when added to the SED for clarification. For lower frequencies up to the peak of both black-body spectra, the spectral index  $\alpha$  equals two according to the Rayleigh-Jeans approximation, Equation (3.5). In the added SED, in line with the peak of the dust spectrum,  $\alpha \neq 2$ .

If  $\alpha \approx 2$  we can proceed to calculate the temperature of the star. Since  $I_\nu = B(\nu, T)$ , we obtain with Equation (3.5) the temperature

$$T = \frac{I_\nu c^2}{2k_B \nu^2}. \quad (3.10)$$

Since dust also emits as a black-body and therefore would not necessarily affect  $\alpha$  (and since we only have two data points) Equation (3.10) is not a reliable estimate for the temperature of the star,  $T_{star}$ . However, if we have data on the temperature of the star and our calculated temperature from  $I_\nu$  with Equation (3.10) is higher than this, we can suppose the temperature difference to originate from the dust intensity, i.e.  $I_{dust} = I_\nu - B(\nu, T_{star})$ .

If  $\alpha$  deviates significantly from 2, it would indicate that the SED differs from a pure black-body spectrum. This could be due to dust. If the observed intensity is higher than the expected intensity with given temperature, distance and luminosity, the dust intensity can be calculated as before,  $I_{dust} = I_\nu - B(\nu, T_{star})$ . According to [19] we can then calculate the total mass of the dust in the CSE in solar masses, for all  $\alpha$ , with the distance to the star in cm,  $D_{star}$ , the frequency dependent opacity of the dust in  $\text{g}/\text{cm}^2$ ,  $\kappa_\nu$ , and the assumed temperature of the dust in K,  $T_{dust}$ , as

$$M_{dust} = \frac{I_{dust} D_{star}^2}{\kappa_\nu B(\nu, T_{dust}) M_\odot}. \quad (3.11)$$

If we assume constant spherical symmetrical expansion and therefore a density distribution  $\rho \propto r^{-2}$ , we can estimate the *dust* mass-loss rate. Due to the assumptions, one spherical shell with radius  $dr$  will contain the same amount of mass everywhere in the CSE. If we also assume the radius of the CSE to  $r_{cse}$ , we can calculate the fraction of the entire CSE-mass leaving the star per unit time with the velocity  $v_{exp}$  with

$$\dot{M}_{dust} = M_{dust} \frac{v_{exp}}{r_{cse}}. \quad (3.12)$$

Finally, we can estimate the gas to dust ratio, since we have assumed the same expansion velocities for both dust and gas, with  $\dot{M}_{gas}$  from Equation (3.8) as

$$g_{gd} = \frac{\dot{M}_{gas}}{\dot{M}_{dust}}. \quad (3.13)$$

# 4

## Observations and Data Analysis

In this chapter, we first present the sample of stars as well as observational specifications of these. We also describe our working methods, including gathering of information and analysing the data.

### 4.1 The sample of stars

The stars analysed in this thesis, Y Hya, U Hya, R For, R Hya and R Crt are presented in 4.1 where some basic properties for the stars relevant for our thesis are found. The sample of stars was chosen by our supervisors from data originating from the DEATHSTAR project[1] and have been calibrated by Wouter Vlemmings of Chalmers University (Professor and Head of Unit, Department of Space, Earth and Environment, Astronomy and Plasma Physics, Galactic Astronomy) before it was provided to us.

**Table 4.1:** Relevant data for the stars used in this thesis. Distance  $D$ , temperature  $T$ , Luminosity  $L$ , stellar radius  $R$ , expansion velocity  $v_{exp}$  and gas mass-loss rate  $\dot{M}$ . The horizontal line between R For and R Hya separate the carbon (above) and oxygen (below) rich stars. The values for Y Hya are from [3], and the rest are from [4].

Star \ Parameter	$D$ [pc]	$T$ [K]	$L$ [ $L_{\odot}$ ]	$R$ [au]	$v_{exp}$ [km s $^{-1}$ ]	$\dot{M}$ [ $10^{-7} M_{\odot} yr^{-1}$ ]
Y Hya	350	2600	4200	1.49	9.0	1.9
U Hya	160	2400	2500	1.34	5.0	0.8
R For	610	2000	5800	2.95	15.5	11
R Hya	150	2600	7700	2.01	6.0	2.1
R Crt	170	2800	4000	1.25	10.0	5.5

### 4.2 Observations

In Table 4.2a and Table 4.2b the observational specifications for all stars in Band 6 and Band 7 respective are presented. The specifications are gathered from their respective files found with the observational data in the ALMA archive [20]. The Y Hya measurements in Band 7 are a combination of data from two different observations and are presented with the setup information for both.

**Table 4.2:** Observational specifications in Band 6 (a) and Band 7 (b) of ACA ALMA. In (b) the Y Hya measurements were taken at two different times and combined into one in the archive, with data for both observations are given. The information was gathered from the corresponding files found in the ALMA Archive. Resolution is the number of baselines and antennas during the observation.

(a)

Parameter \ Star	Y Hya	U Hya	R For	R Hya	R Crt
Calibrators	'Callisto', 'J1037-2934', 'J1058+0133', 'J1256-0547'	'J1037-2934' 'J1048-1909' 'J1058+0133'	'J0137-2430' 'J0510+1800' 'J0522-3627' 'Mars'	'Callisto' 'J1256-0547' 'J1336-3357' 'J1351-2912'	'J1037-2934' 'J1048-1909' 'J1058+0133'
Observation time	0:16:08	0:16:38	0:16:38	0:16:08	0:16:38
minimum baseline	8.9 m	8.9 m	8.9 m	8.9 m	8.9 m
maximum baseline	48.0 m	48.0 m	48.0 m	48.0 m	48.0 m
Resolution	55,11	55,11	55,11	55,11	55,11
Date, time (UTC)	2017-05-21, 00:04:55	2017-05-15, 21:39:37	2017-05-14, 17:24:36	2017-05-21, 01:06:40	2017-05-15, 21:39:37

(b)

Parameter \ Star	Y Hya	U Hya	R For	R Hya	R Crt
Callibrations	'J0854+2006' 'Ganymede' 'J1037-2934' 'J1037-2934' 'J1058+0133' 'J1229+0203'	'J1048-1909' 'J1058+0133'	'J0006-0623' 'J0137-2430' 'Uranus'	'Ganymede' 'J1246-2547' 'J1256-0547'	'J1048-1909' 'J1058+0133'
Observation time	0:22:11   0:22:11	0:22:11	0:11:05	0:22:11	0:22:11
minimum baseline	8.9 m   9.4 m	8.9 m	8.9 m	8.9 m	8.9 m
maximum baseline	48.0 m   48.0 m	48.0 m	48.0 m	48.0 m	48.0 m
Resolution	55,11   36,9	55,11	45,10	55,11	55,11
Date, time (UTC)	2017-05-14, 20:57:38   2017-06-23, 21:33:47	2017-05-14, 22:36:43	2017-05-17, 13:26:30	2017-05-16, 00:39:05	2017-05-14, 22:36:43

### 4.3 Information gathering

The information used in this report came mainly from three sources: [7], [8] and [2]. The first two were given to us by our supervisors. The third, together with all other references in this thesis, were found by searching in large databases such as Web of Science, Google Scholar, Chalmers library and astrophysics data systems and sorting for the most cited.

### 4.4 Data analysis

As mentioned in Section 3.5, the data was structured in two different formats. The first (type 1) was a spectral cube where the  $x$  and  $y$  coordinates corresponded to spatial coordinates in degrees centred around the star. The  $z$  coordinate represents a frequency bin with a width of a few 100 kHz covering around 1 GHz in total for all  $z$ . For each pixel with coordinates  $x$ ,  $y$  and  $z$  the observed intensity in Jy/beam was given. The other format (type 2) was an image with the same  $x$  and  $y$  coordinates but for a larger bin of about 10 GHz, the continuum image. In Band 6 and Band 7 there were four different (eight in total) frequency spans of the first types approximately centred around the rest frequency of common CSE molecules and one (two in total) of the second type. The detailed frequency spans are displayed in Table 4.3 and are representative for all stars.

The primary software used for the analysis was MATLAB, in which we created our own scripts for our purposes. We also used CASA to illustrate the data and check if emission lines were

spatially resolved.

#### 4.4.1 Integrated flux density

Depending on the angular resolution of the telescope and the size of the astronomical object, an object may be either resolved or unresolved. The two methods used for calculating the flux density of the spectrum was either by using the centre pixel of the source emission when studying a source smaller than the synthesised beam<sup>1</sup> (an unresolved source), or by using a larger aperture, which is covering the entire source (if the source is resolved). When using the centre pixel for a point source, the Jy/beam provided from the observational data is the same as the peak flux value in Jy. For an aperture, the conversion from the Jy/beam data to Jy was made by dividing the summed flux in the aperture by the number of pixels in the synthesised Gaussian beam.

Using CASA to analyse the image component size in several spectral windows, the conclusion was that results vary. Depending on the molecular species and transition, the emission from the spectral lines may or may not be resolved. HC<sub>3</sub>N in Y Hya, for example, was most likely unresolved, with the image component size convolved with the beam being  $\sim 5\%$  smaller than the beam size. This is also seen as the integrated flux density over an aperture is  $\sim 2\%$  lower than the centre pixel integrated flux, well within the uncertainty of the noise (see Section 6.1.2). Comparisons can also be made with <sup>12</sup>CO  $J = 2 \rightarrow 1$  in Y Hya which was most likely resolved, with the image component size convolved with the beam being  $\sim 70\%$  larger than the beam size. This was even more clear when looking at the difference in integrated flux density over an aperture larger than the object, against the centre pixel, resulting in  $\sim 53\%$  more flux when integrating over an aperture larger than the *full width at half maximum* (FWHM) of the image component. Therefore, the conclusion was that the aperture should be used when analysing resolved sources.

A risk of using the method of summing all pixels in an aperture around the source is that if the aperture is made too large, there would be an increased sensitivity to artefacts in the image. While the noise of the spectrum decrease with the averaging effects of the aperture, the probability of including artefacts increase. Even though the risk is lower, artefacts could affect centre pixel calculations as well; we might not be aware of them. To minimise the risk of any additional errors, the centre pixel was used in the analysis of the emission continuum files as the source emission was determined to be unresolved, and when the aperture was used, it was minimised in size while still including the entire source.

---

<sup>1</sup>The interferometer equivalent of single dish beam.

**Table 4.3:** Frequency ranges of the data, see text for details. The name for the type 1 files roughly corresponds to a specific transition with that molecule in its frequency range. CONT is the name of the continuum files, type 2. The line halfway through separate the files in Band 6 and Band 7.

Name	Type	Frequency range [GHz]	Bin size [km/s]
SiO	1	215.4 - 217.4	1.5
SiS	1	217.3-219.3	1.5
<sup>12</sup> CO	1	230.2-231.2	0.75
SO <sub>2</sub>	1	231.1-233.1	1.5
CONT	2	224.3-241.9	-
<sup>13</sup> CO	1	330.3-331.3	0.75
SO <sub>2</sub>	1	331.3-333.3	1
CS	1	342.5-344.5	1
<sup>12</sup> CO	1	345.1-346.1	0.75
CONT	2	338.2-354.0	-

#### 4.4.2 Emission lines

On examination of the studied molecular gas emission lines, a large number was found to be resolved. This resulted in the decision to employ the same method of integrating the flux densities with the sum over an aperture across all analysis of gas emission lines.

##### 4.4.2.1 Gas mass-loss rate

Calculations of the gas mass-loss rates were performed using Equation (3.8). Variables acquired from the data were the expansion velocity  $v_{exp}$ , beam size  $\Theta_b$  and velocity integrated intensity of the CO-line  $I_{CO}$ . The expansion velocity  $v_{exp}$  was determined from the <sup>12</sup>CO  $J = 2 \rightarrow 1$  emission line by taking half the width of the line at  $5\sigma$  from the average noise level. Since an aperture was used to calculate the flux density, the beam size used was the radius of a circle with area  $A_{circle} = A_{aperture}$ . Lastly, the mass loss-rate formula requires a velocity integrated intensity in units  $\text{K km s}^{-1}$ .<sup>2</sup> Using the ALMA Observation tool, a Jy→K conversion factor of 0.7 was obtained for the data. The conversion is dependent on the synthesised beam, and any deviation in beam size could affect this factor. For this reason, the aperture used for calculating the flux density was sized as tightly as possible to the beam while still covering the entire resolved source.

##### 4.4.2.2 Molecular identification

When detecting molecular lines in the spectral data, the method has to deal with both identifying the line intensity over the noise as well as the exact positioning of the line. Therefore, our method consists of first determining the existence of a line through analysis of the signal to noise ratio and then finding the appropriate molecular transition through a selection process based on theoretical knowledge of AGB stars.

<sup>2</sup>Single dish telescopes measure intensity in terms of antenna temperature in K while interferometers measure in Jy.

Assuming that the noise is primarily random, to determine a line with high certainty, we define that the peak needs to be larger than five standard deviations,  $5\sigma$ , of the noise. In most of the more common molecular transitions such as  $^{12}\text{CO } J = 2 \rightarrow 1$ , the emission line was very distinguishable without any further analysis. In situations when this was not the case, signal averaging of the spectrum in combination with an optimised aperture was used to spot some of the weaker spectral lines.

Once a molecular transition had been located, the Doppler shift was accounted for, effectively moving the intensity peak to the rest frequency. The located frequency is studied using the Splatalogue<sup>3</sup> [18]. A narrow frequency interval less than the Doppler shift is studied, and if no molecules that are common in AGB stars [8] are found, further analysis is needed. For example, effects like maser can be a factor that shifts the located emission line; this is further discussed in Section 6.2.

### 4.4.3 Continuum emission

When examining the continuum emission data with CASA for Y Hya, U Hya, R For, and R Hya, the source emission was determined to be unresolved or only marginally resolved in one direction. In all of these cases, therefore, the centre pixel method of obtaining the flux of the emission has been used. However, in the continuum emission data of R Crt (band 7), the emission was determined to possibly be slightly resolved in one direction, with an image component size convolved with the beam  $\sim 5\%$  larger than the beam size. After examining both the aperture and the centre pixel approach to determine the flux, the variance in results were less than  $\sim 5\%$ , concluding that the centre pixel method was accurate for the entire sample of stars. Using the calculated flux, the spectral index was calculated for all stars with Equation (3.9).

Using the distance, radius and temperature in Table 4.1 a black-body spectrum was fitted for all stars, and the expected fluxes for the centre frequencies were obtained. For the stars with  $\alpha \approx 2$ , which was the case for Y Hya ( $\alpha = 2.09$ ) and R Crt ( $\alpha = 2.09$ ), the temperature was calculated with Equation (3.10). The temperatures achieved for Band 6 and Band 7 were similar to those in the literature, Table 4.1, for both stars. In line with Section 3.5.2, no further analysis of the dust was made.

For the stars with  $\alpha \neq 2$  (U Hya, R For and R Hya) the expected fluxes were compared to the measured fluxes. If the measured fluxes were  $> 10\%$  than the expected, we considered it significant, and it was assumed to be due to dust. The mass of the dust and the dust mass-loss rate was then calculated (for R For and R Hya) with Equation (3.11) and Equation (3.12) using a dust temperature of 100 K as a typical value [8], since we do not have any further information on it. The input CSE radii was  $r_{cse} = 8 \cdot 10^{16}$  cm for R For[3] and  $r_{cse} = 1.2 \cdot 10^{16}$  cm for R Hya[21]. The opacities used for Band 6 and Band 7 for the carbon-rich stars was assumed as  $\kappa_{B6} = 1.11 \text{ g/cm}^2$   $\kappa_{B7} = 2.03 \text{ g/cm}^2$  and for the oxygen-rich stars  $\kappa_{B6} = 0.35 \text{ g/cm}^2$   $\kappa_{B7} = 0.76 \text{ g/cm}^2$ .

---

<sup>3</sup> Splatalogue is a database for astronomical spectroscopy that contains over 5.8 million lines in submillimeter, millimetre, and microwave range.

# 5

## Results

In this chapter we present our obtained results from the data analysis as discussed in Section 4.4. First, we show the results for all stars from the emission lines; the gas mass-loss rates in Band 6 and Band 7, and the identified molecules. Second, the results from the continuum emission is presented. For both the emission lines and the continuum spectra, figures of the data collected for the emission lines are also presented.

### 5.1 Emission lines

Here we present the results calculated from for  $\dot{M}_g$ , tabulated with literature values for comparison. We also present the results from the error analysis, as well as the change in  $\dot{M}_g$  when changing all the parameters in equation 3.8. This part also contain all the results gathered from the molecular line analysis.

#### 5.1.1 Mass loss-rate

**Table 5.1:** Values from the literature (*column 2-3*) and measured values (*column 4-5*) of the expansion velocity and the gas mass-loss rates (Equation (3.8)) for all stars in our sample. Two values for our measured gas mass-loss rate (*column 5*) are presented where the *top* value is  $J = 2 \rightarrow 1$  (Band 6) and the *bottom* value  $J = 3 \rightarrow 2$  (Band 7). The literature values are the same as those in Table 4.1. The double line between R For and R Hya separate the carbon stars (*above*) from the oxygen stars (*below*).

Star	Literature Values		Measured Values	
	$v_{exp}$ [kms <sup>-1</sup> ]	$\dot{M}$ [10 <sup>-7</sup> M <sub>⊙</sub> yr <sup>-1</sup> ]	$v_{exp}$ [kms <sup>-1</sup> ]	$\dot{M}$ [10 <sup>-7</sup> M <sub>⊙</sub> yr <sup>-1</sup> ]
Y Hya	9.0	1.9	9.2	4.1 ( $J = 2 \rightarrow 1$ ) 3.0 ( $J = 3 \rightarrow 2$ )
U Hya	5.0	0.8	7.5	2.8 ( $J = 2 \rightarrow 1$ ) 2.4 ( $J = 3 \rightarrow 2$ )
R For	15.5	11	19	24 ( $J = 2 \rightarrow 1$ ) 22 ( $J = 3 \rightarrow 2$ )
R Hya	6.0	2.1	11	3.1 ( $J = 2 \rightarrow 1$ ) 4.5 ( $J = 3 \rightarrow 2$ )
R Crt	10.0	5.5	12	6.9 ( $J = 2 \rightarrow 1$ ) 7.4 ( $J = 3 \rightarrow 2$ )

In Table 5.1 the mass-loss rates calculated from the CO  $J = 2 \rightarrow 1$  and  $J = 3 \rightarrow 2$  transitions with the Ramstedt equation and the expansion velocities for the various stars are presented together with values from the literature for comparison.

All the obtained expansion velocities and mass-loss rates are higher than those in the literature. The mass-loss rates are approximately two times higher for Y Hya, R For and R Hya, three times higher for U Hya and  $\approx 40\%$  higher for R Crt. The expansion velocities most noticeably higher for R Hya where our measured value is almost twice as large as that in the literature. For U Hya, R For and R Crt the velocity is a few  $\text{kms}^{-1}$  larger while Y Hya have practically the same value as in the literature.

We notice that higher expansion velocities corresponds to higher mass-loss rates for all examined stars. U Hya has the lowest expansion velocity of  $v_{exp} = 7.5 \text{ kms}^{-1}$  and the lowest mass-loss rate of  $\dot{M}_{J=3 \rightarrow 2} = 2.4 \cdot 10^{-7} M_{\odot} \text{ yr}^{-1}$  and R For the highest with  $v_{exp} = 19 \text{ kms}^{-1}$  and  $\dot{M}_{J=2 \rightarrow 1} = 24 \cdot 10^{-7} M_{\odot} \text{ yr}^{-1}$ .

The convergence between  $\dot{M}_{J=2 \rightarrow 1}$  and  $\dot{M}_{J=3 \rightarrow 2}$  are rather similar for most stars with a maximum difference for R Hya of about 30% between the largest and smallest value. For the carbon stars,  $\dot{M}_{J=2 \rightarrow 1}$  gives the larger mass-loss rate while the opposite is true for the oxygen stars.

Out of the five used parameters in the Ramstedt formula, an error estimation has been performed for three; CO-line intensity ( $I_{CO}$ ), distance to the star ( $D$ ), expansion velocity ( $v_{exp}$ ), presented in Table 5.2b. The remaining two variables, the beam size,  $\Theta_b$ , and CO/H-ratio,  $f_{CO}$ , are not treated as error parameters in our usage of the formula.  $\Theta_b$  is assumed to be true and the aperture used in the formula is calculated without uncertainty. The values of  $f_{CO}$  are assumed by Ramstedt when formulating the mass-loss rate estimator[2], and any errors of this parameter will be assumed to fall under the uncertainty of the formula itself.

In Table 5.2a the mass-loss rate dependence on each of the five parameters is presented with a general  $\pm 50\%$  variation to illustrate the sensitivity of the formula to the individual parameters.

Provided with the information from Table 5.2a we can get the extreme values of the mass-loss rate. This is done by adding the values together, first the positive increase and then the negative decrease. Doing this gives us  $+79\%$  and  $-66\%$  for the given method, that is how much the uncertainty of the parameters affect the result. This can be seen as a very rough estimate of our error margin. It is not an error estimate which contains the inherent errors from the method Ramstedt used to validate the equation, but only a way of seeing how our estimated errors of the parameters used changes the equation.

### 5.1.2 Molecular catalogue

The identified molecular transitions that were located in all studied stars can be found in Table 5.3. Here we present the molecule, the transition and the corresponding rest frequency in GHz, the peak intensity of the line, the velocity resolution, the total integrated flux and the size of the aperture used. A total of fifty transitions for fifteen molecules were identified. We notice that the molecules, CO,  $^{13}\text{CO}$ ,  $\text{H}^{13}\text{CN}$  and SiO are located in all stars. Out of the fifteen identified molecules, eleven are diatomic, three contain three atoms, and one has five. The discrepancies between carbon- and oxygen-rich stars are quite apparent since nine out of the fifteen molecules in total was identified in the carbon-rich stars and eight in the oxygen-rich leaving six molecules found in both spectral types. In Appendix B

**Table 5.2:** Studying the Ramstedt mass-loss formula, five variable dependencies can be recognised affecting the result of the calculated mass-loss; CO-line intensity ( $I_{CO}$ ), beam size ( $\Theta_b$ ), distance to the star ( $D$ ), expansion velocity ( $v_{exp}$ ), CO abundance ( $f_{CO}$ ). The CO  $J = 3 \rightarrow 2$  parameters were used, as they yielded the highest extreme value when adding up the different errors. In (a), each parameter is varied by  $\pm 50\%$  accompanied by the corresponding variation in mass-loss rate. In (b), each parameter is instead varied according to the constraints from the analysed uncertainty in Section 6.1.

(a)

Parameter	Change	$\dot{M}$
$I_{CO}$	+ 50 %	+ 45 %
	- 50 %	- 47 %
$\Theta_b$	+ 50 %	+ 109 %
	- 50 %	- 72 %
$D$	+ 50 %	+ 109 %
	- 50 %	- 72 %
$v_{exp}$	+ 50 %	+ 17 %
	- 50 %	- 24 %
$f_{CO}$	+ 50 %	- 17 %
	- 50 %	+ 37 %

(b)

Parameter	Change	$\dot{M}$
$I_{CO}$	+ 15 %	+ 14 %
	- 15 %	- 14 %
$\Theta_b$	+ 0 %	+ 0 %
	- 0 %	- 0 %
$D$	+ 30 %	+ 61 %
	- 30 %	- 47 %
$v_{exp}$	+ 10 %	+ 4 %
	- 10 %	- 4 %
$f_{CO}$	+ 0 %	- 0 %
	- 0 %	+ 0 %

figures are shown presenting all identified molecules with their transitions marked on the corresponding rest frequency for all five stars. We also note that molecules including C is more commonly occurring in C-rich stars and molecular compositions including O is more commonly occurring in O-rich stars. It is noteworthy that AlO was identified in R Crt since it was only recently discovered in an AGB star (2016) [6].

**Table 5.3:** Identified molecular lines for the five studied stars, the molecule and the transitions with its rest frequency are presented.  $I_{\nu,peak}$  is the flux peak,  $\Delta v$  is the bin size,  $\int I_{\nu} d\nu$  is the integrated flux over the located peak and  $\theta$  is the size of the aperture. The name of the transitions are from the Splatalogue[18]. For a summary of the identified molecules see Table 6.1. Note that this table cover multiple pages.

Molecule	Transition	Restfreq. [GHz]	Star	$I_{\nu,peak}$ [Jy]	$\Delta v$ [km s <sup>-1</sup> ]	$\int I_{\nu} d\nu$ [Jy km s <sup>-1</sup> ]	$\theta$ ["]
CO	2 $\rightarrow$ 1	230.5380	Y Hya	10.5	0.75	136	9
			U Hya	39.6	0.75	402	8
			R For	11.3	0.75	317	8
			R Hya	23.9	0.75	251	8
			R Crt	25.2	0.75	423	8
	3 $\rightarrow$ 2	345.7960	Y Hya	17.1	0.75	208	5
			U Hya	54.3	0.75	563	5
			R For	20.0	0.75	526	5
			R Hya	59.7	0.75	679	5
			R Crt	39.8	0.75	654	5

Continued on next page

5. Results

Table 5.3 – continued from previous page

Molecule	Transition	Restfreq. [GHz]	Star	$I_{\nu,peak}$ [Jy]	$\Delta v$ [km s <sup>-1</sup> ]	$\int I_{\nu} d\nu$ [Jy km s <sup>-1</sup> ]	$\theta$ ["]
<sup>13</sup> CO	3 → 2	330.5880	Y Hya	0.575	0.75	4.22	6
			U Hya	4.89	0.75	40.0	5
			R For	1.04	0.75	16.6	5
			R Hya	1.92	0.75	21.1	5
			R Crt	4.43	0.75	46.6	5
H <sup>13</sup> CN	4 → 3	345.3398	Y Hya	1.21	0.75	9.38	5
			U Hya	4.13	0.75	27.3	5
			R For	2.43	0.75	49.4	5
			R Hya	0.958	0.75	3.78	5
			R Crt	2.29	0.75	33.4	5
SiO	5 → 4	217.1050	Y Hya	0.439	1.5	3.41	9
			U Hya	0.0938	1.5	0.932	8
			R For	2.32	1.5	53.1	8
			R Hya	26.5	1.5	166	8
			R Crt	24.1	1.5	328	8
SiO v=1	5 → 4	215.5959	R Hya	6.99	1.5	55.0	8
			R Crt	5.18	1.5	40.8	8
<sup>29</sup> SiO	8 → 7	342.9808	R For	0.473	1	9.14	4
			R Hya	12.6	1	55.6	5
			R Crt	7.84	1	102	5
SO <sub>2</sub>	4(3, 1) → 3(2, 2)	332.5052	R Crt	0.932	1	13.4	5
	21(2, 20) → 21(1, 21)	332.0914	R Crt	0.461	1	5.38	5
	22(2, 20) → 22(1, 21)	216.6433	R Crt	0.291	1.5	3.36	8
	34(3, 31) → 34(2, 32)	342.7616	R Crt	0.230	1	1.23	5
SiS	12 → 11	217.8177	R For	0.216	1.5	3.27	8
SO	8(8) → 7(7)	344.3106	R Hya	1.38	1	7.21	5
			R Crt	3.09	1	49.4	5
<sup>34</sup> SO	6(5) → 5(4)	215.8399	R Crt	0.193	1.5	2.89	8
HC <sub>3</sub> N	24 → 23	218.3248	Y Hya	0.235	1.5	1.84	9
			U Hya	0.418	1.5	6.86	8
CS	7 → 6	342.883	Y Hya	4.41	1	36.5	7
			U Hya	1.08	1	9.16	7
			R For	6.65	1	148	7
			R Hya	0.188	1	0.467	7
<sup>13</sup> CS	5 → 4	231.221	Y Hya	0.158	1.5	0.272	8
			R For	1.171	1.5	4.03	8
SiC <sub>2</sub>	10(2, 9) → 9(2, 8)	232.5341	Y Hya	0.715	1.5	5.38	8
			R For	0.405	1.5	8.00	8
	15(2, 14) → 14(2, 13)	342.8050	Y Hya	0.651	1	4.33	5
			R For	0.271	1	6.18	4
	14(6, 8) → 13(6, 7)	330.8705	Y Hya	0.689	0.75	4.26	6
	14(6, 9) → 13(6, 8)	330.8745					
			R For	0.427	0.75	4.74	5
AlO	9(19/2, 10) → 8(17/2, 9)	344.463	R Crt	0.208	1	1.45	5
	9(19/2, 6) → 8(17/2, 6)						

Continued on next page

Table 5.3 – continued from previous page

Molecule	Transition	Restfreq. [GHz]	Star	$I_{\nu,peak}$ [Jy]	$\Delta v$ [km s <sup>-1</sup> ]	$\int I_{\nu} d\nu$ [Jy km s <sup>-1</sup> ]	$\theta$ [ $''$ ]
<sup>13</sup> CN	217.2646 → 217.3152 GHz		U Hya	0.164	1.5	1.82	8
			R For	0.198	1.5	4.53	8
	217.4286 → 217.4968 GHz		U Hya	0.192	1.5	2.91	8
			R For	0.137	1.5	3.46	8

The transitions found in all five stars (CO(2 → 1), CO(3 → 2), <sup>13</sup>CO(3 → 2), H<sup>13</sup>CN(4 → 3) and SiO(5 → 4)) are shown in Figure 5.1. In Figure 5.2, other transitions not found in all stars are presented in no particular order. Fine structure transitions, which contain a splitting of a line and therefore have two separate peaks, are shown in Figure 5.3.

Two fine structure transitions for <sup>13</sup>CN identified in U Hya and R For have several lines in a narrow interval; these are presented in Figure 5.4. The two graphs on the left side of the figure contain sixteen lines, and the two graphs on the right twelve lines. It can be seen by the indication of the red lines that the measured flux follows the expected relative flux.

## 5.2 Continuum emission - dust

In Table 5.4 the results from the continuum emission are presented for all stars. The measured flux  $I$  in Band 6 and Band 7 can be seen together with the spectral index  $\alpha$ , expected flux  $I'$ , temperature  $T'$ , dust flux  $F_D$ , dust mass  $M_D$  and dust mass-loss rate  $\dot{M}_D$ . For the stars with  $\alpha \approx 2$ , Y Hya and R Crt,  $I$  is within 15% of  $I'$ . Their calculated temperature, according to Equation (3.10), are similar to those given by the literature in Table 4.1 where for Y Hya  $T = 2600$  and for R Crt  $T = 2800$ .

For U Hya we note that the measured flux is almost half of what is expected and that its spectral index deviates from 2 as  $\alpha = 1.70$ .

For R For and R Hya, the spectral indices both deviate from 2 and especially so for R For with  $\alpha = 1.30$ . These stars also have higher measured flux than expected from a pure black-body spectrum where both bands for R For and Band 6 for R Hya satisfy  $F_D \gtrsim 0.15F$ . The resulting dust masses are in the same order of magnitude for both stars while the dust mass-loss rate is one order of magnitude lower for R For for both bands.

**Table 5.4:** The measured flux  $I$  (*column 3*) and the obtained values from calculations with the measured flux and/or literature values from Table 4.1 (*column 4-9*): Spectral index  $\alpha$ , expected flux  $I'$ , temperature  $T'$ , flux of dust  $I_D$  ( $I_D = I - I' \gtrsim 0.10F$ ), the logarithm of the dust mass  $M_D$  and the logarithm of the dust mass-loss rate  $\dot{M}_D$ . All values except  $\alpha$  are given for the two Bands (*column 2*): Band 6 (*above*) and Band 7 (*below*).

Star	Band	$I$ [mJy]	$\alpha$	$I'$ [mJy]	$T'$ [K]	$I_D$ [mJy]	$M_D$ [ $\log(M_\odot)$ ]	$\dot{M}_D$ [ $\log(M_\odot yr^{-1})$ ]
Y Hya	6	4.7	2.09	5.3	2300	-	-	-
	7	11.0		12.1	2400	-	-	-
U Hya	6	11.1	1.70	19.3	-	-	-	-
	7	22.3		43.9	-	-	-	-
R For	6	8.1	1.30	5.3	-	2.8	-5	-8
	7	13.8		12.1	-	1.7	-5	-8
R Hya	6	60.8	1.78	53.2	-	7.5	-5	-7
	7	126.3		120.9	-	-	-	-
R Crt	6	16.9	2.09	17.2	2700	-	-	-
	7	39.9		39.2	2800	-	-	-

## 5. Results

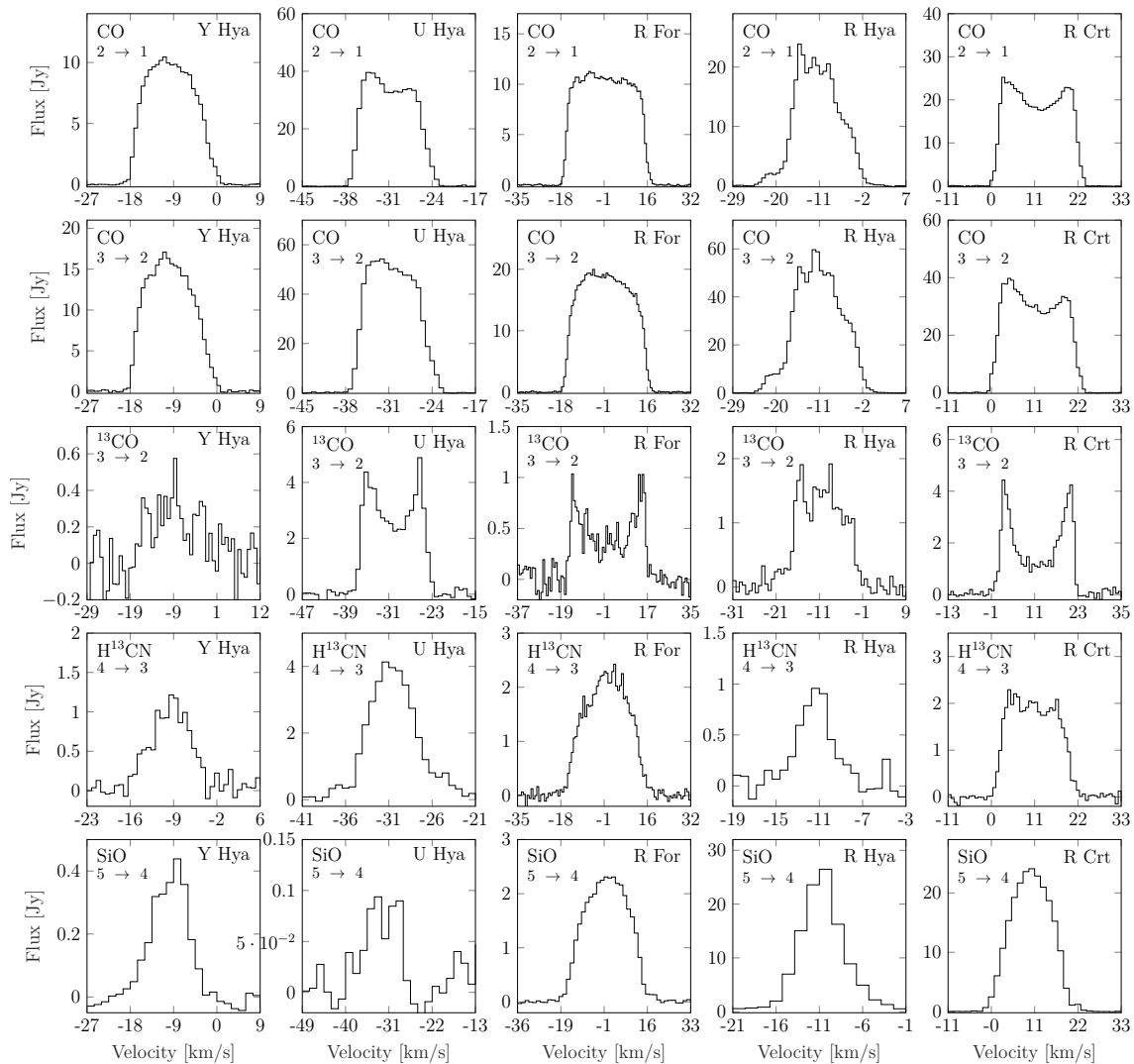


**Figure 5.1:** Molecular transitions that have been identified in all five studied stars, CO( $2 \rightarrow 1$ ), CO( $3 \rightarrow 2$ ),  $^{13}\text{CO}$ ( $3 \rightarrow 2$ ), H $^{13}\text{CN}$ ( $4 \rightarrow 3$ ) and SiO( $5 \rightarrow 4$ ). In the *top left corner* of each graph, the chemical name and its transition is indicated. In the *top right corner*, we see the name of the star. The *y-axis* show the flux in Jy while the *x-axis* display the unshifted velocity in  $\text{km s}^{-1}$  where  $0 \text{ km s}^{-1}$  correspond to the rest frequency. The integrated flux of each line can be found in Table 5.3.

## 5. Results

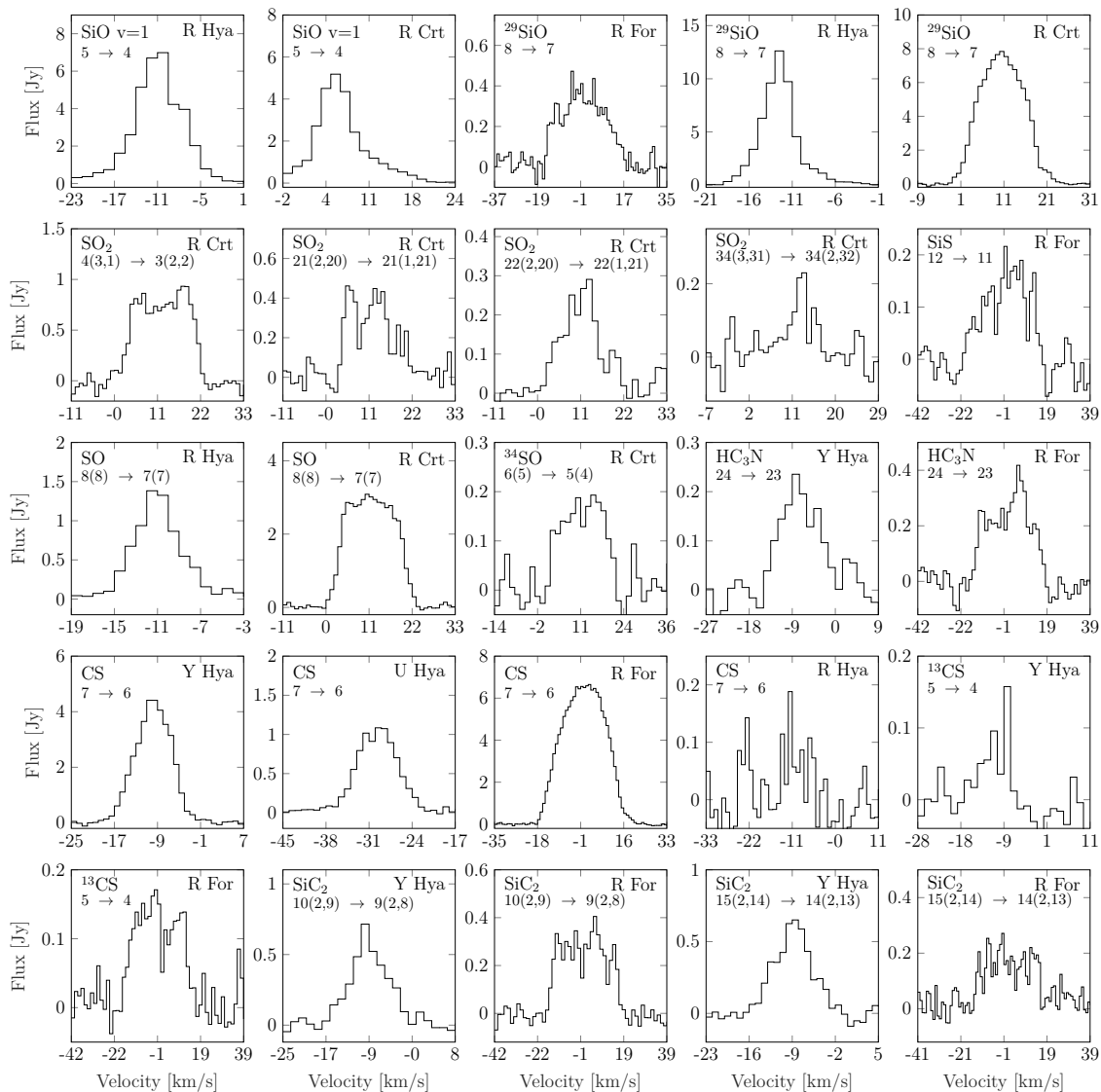


**Figure 5.2:** Single molecular transition that has been identified in less than five stars. In the *top left corner* of each graph, the chemical name and its transition is indicated. In the *top right corner*, we see the name of the star. The *y-axis* show the flux in Jy while the *x-axis* display the unshifted velocity in  $\text{km s}^{-1}$  where  $0 \text{ km s}^{-1}$  correspond to the rest frequency. The integrated flux of each line can be found in Table 5.3.

## 5. Results

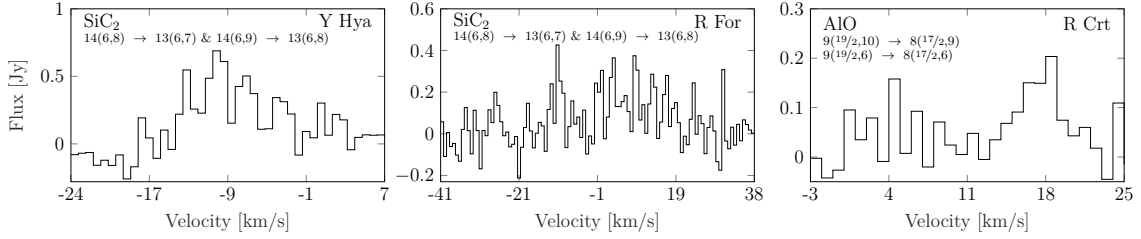


**Figure 5.3:** Molecular transitions that have two narrow lines contributing to the same peak. In the *top left corner* of each graph, the chemical name and its transition is indicated. In the *top right corner*, we see the name of the star. The *y-axis* show the flux in Jy while the *x-axis* display the unshifted velocity in  $\text{km s}^{-1}$  where  $0 \text{ km s}^{-1}$  correspond to the rest frequency. The integrated flux of each line can be found in Table 5.3. On the third graph is the AlO line which is a recently discovered molecule in AGB stars. The integrated flux of each transition can be found in Table 5.3.

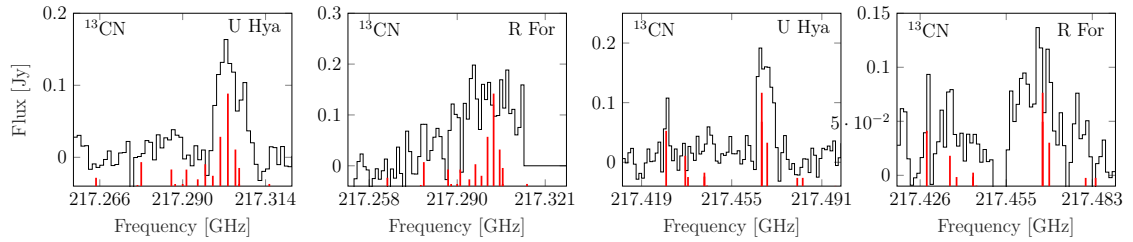


**Figure 5.4:** Molecular lines for <sup>13</sup>CN in the stars U Hya and R For. The two graphs on the *left* ( $217.2646 \rightarrow 217.3152 \text{ GHz}$ ) has sixteen lines and the two on the *right* ( $217.4286 \rightarrow 217.4968 \text{ GHz}$ ) have twelve lines. The position of the *red* lines indicate where the separate transitions should be found and their height represent the expected flux relative to each other. It can be noted that the measured flux follows the expected relative flux. The integrated flux of each line can be found in Table 5.3.

# 6

## Discussion and Conclusions

We end this thesis by discussing our results and presenting our conclusions — both general and stellar specific.

### 6.1 Gas mass-loss rate

Here we discuss the accuracy of the obtained gas mass-loss rate estimates. We present the dependence on variables which serves to indicate how sensitive Equation (3.8) is to uncertainties in its input-parameters. The result of these uncertainties are those presented in Table 5.2b. Finally we discuss the obtained values of  $\dot{M}$ .

The use of Ramstedt's mass-loss rate formula requires parameters in the ranges  $10^{-7} \leq \dot{M} \leq 10^{-5} M_{\odot} \text{ yr}^{-1}$ ,  $5 \leq v_{exp} \leq 20 \text{ km s}^{-1}$  and  $10^{-4} \leq f_{CO} \leq 10^{-3}$ . Our results satisfy all these conditions. Furthermore, the equation has been validated by Ramstedt in [2] and it is stated that the formula will estimate the mass-loss rate within a factor of three in comparison to radiative transfer modelling[2]. The assumed  $f_{CO}$  parameter is included in this error why we do not discuss its uncertainty ( $\pm 0\%$ ).

#### 6.1.1 Distance measurement - $D$

The approximation of the uncertainty in distance is based on the variance in distance measurements that we found in previous studies of the stars. Specifically, we performed a comparison of distances found in [1, 21, 4, 22, 3] where both a (P-L) and a parallax method was used. By looking at the variance from the average of these five independent distance calculations, an extreme of  $-18\%$  and  $+23\%$  was found. As the parallax method itself is flawed for AGB stars, one cannot be certain that any of the parallax measurements provide an accurate calculation of the true distance. However, looking at parallax distances in combination with (P-L) distances could give an uncertainty interval covering the possible variation of the parallax method. Also, if the position of the brightest spot of the star could be considered random, analysing several data points could give a rough estimate of a range of possible distances for a star. Therefore, without further analysis of the phenomena which creates the issue with the parallax method and the individual errors of the (P-L) distances, we will assume an error, on the basis of the discussion above and the  $-18\%/+23\%$ -range, of  $\pm 30\%$  for all of our distance measurements.

In a more in-depth comparison of distance estimates and the involved methods, [17] compared their independent distance estimate to earlier calculations, primarily based on the (P-L) method and one using the parallax method. All of the distance estimates were found to be consistent with each other, except the one based on the parallax method, being

approximately 20-30% smaller than the rest. Our uncertainty of  $\pm 30\%$  is then relatively close in size to the discrepancy of the parallax method found in [17], solidifying the argument that our uncertainty is a reasonable approximation of the distance error.

### 6.1.2 CO-line intensity - $I_{CO}$

Here, we will discuss two different errors for the observed flux. Firstly, there is a risk of systematic errors for any interferometric measurement. In contrast to a single-dish telescope, interferometric telescopes do not have a measurable physical quantity, equivalent to the kelvin data obtained by the single-dish. Instead, the interferometer needs to be properly calibrated to objects with known flux, such as quasars, and tested to produce similar results as previous observations in order to remove any systematic errors. The calibrations can be found in Table 4.2a and Table 4.2b and we assume its errors to be negligible for the purpose of this thesis.

The second type of uncertainty is the random error from noise. The noise can be observable in both the full image since the intensity varies where it would be expected to have a constant zero flux, as well as in the spectrum of integrated flux densities over the frequencies. Measuring the  $5\sigma$  standard deviation of the noise gives an indication of how much variance in observed flux can be expected in every data point. To simplify the analysis of the noise, Y Hya has been used as an example. For the image noise of a single frequency, it is  $\sim 9.5\%$ , and for the centre pixel over a range of frequencies in the CO  $J = 3 \rightarrow 2$  line<sup>1</sup>, it is  $\sim 5.3\%$ . However, the higher number in the image noise may be due to imaging artefacts originating in the interferometric method. As mentioned in Section 4.4.1, using a large aperture seem to increase susceptibility to artefacts. The same effect may be what is observed when calculating the noise of the image (using a very large aperture). While the risk of including artefacts outside of the source was minimised by using the smallest possible aperture while still including the entire emission, this error will be added to the approximate uncertainty of the flux. The conclusion is therefore that the total error for the CO-line intensity will be approximately constrained by  $5\sigma_{freq} + 5\sigma_{img} \approx 15\%$ .

### 6.1.3 Beam size - $\Theta_b$

The beam size is a measured quantity which is unique to each interferometric observation. The beam is synthesised from the inverse Fourier transform of the visibility function, see Section 3.1. Since an aperture was used to calculate the velocity integrated intensity, the aperture is the variable used in the mass-loss rate formula as  $\Theta_b$ . The calculated aperture is exact, and therefore no errors will be assumed for this part of the equation.

### 6.1.4 Expansion velocity - $v_{exp}$

To calculate an error estimate for the expansion velocity, we assume that the width of each observed line is accurate to two pixels, each with a given  $\Delta v$  (Table 4.3). Using Y Hya as an example, this translates to an uncertainty of about 8% of the expansion velocity with

<sup>1</sup>The CO  $J = 3 \rightarrow 2$  had a lower signal to noise ratio than the  $J = 2 \rightarrow 1$  line. Therefore, the  $J = 3 \rightarrow 2$  line was used in the analysis of the noise in order to obtain an upper limit to the noise error.

$\Delta v = 0.75 \text{ km s}^{-1}$  and  $v_{exp} = 9.2 \text{ km s}^{-1}$ . Therefore, a similar error of  $\sim 10\%$  will be assumed for all stars.

### 6.1.5 Obtained gas mass-loss rates

The error estimates of our values for  $\dot{M}$  that are presented in Table 5.2b give an uncertainty of +79% and -66%. If we compare this range with the factor three (+300%/-67%) related to the Ramstedt formula, we get a sense of what error makes the largest contribution. For the upper limit, it is the Ramstedt formula that represents the largest uncertainty; however for the lower limits, the errors are of equal weight. Therefore, we could improve our estimates with the Ramstedt equation if we could reduce our error margin in its input-parameters. It is the distance parameter that creates the largest variation in  $\dot{M}$  (+%/-%) why the accuracy of our result would benefit the most from more precise distance estimates. Perhaps, implementation of the method used by [17] could be used in further studies to reduce uncertainty.

All values that we have calculated of  $\dot{M}$ , presented in Table 5.1, are within the mentioned factor three for the Ramstedt equation. However, our mass-loss rates are consistently higher with  $\sim 40 - 250\%$ , which, even though a sample of five stars is not enough to draw definite conclusions, could indicate a systematic error.

One possible explanation is that the Ramstedt equation is modelled with data from single-dish telescopes, while the data we have used is from an interferometer. Since we have to construct an aperture to integrate the flux, for which the corresponding beam size  $\Theta_b$  is used as an input parameter in Equation (3.8), errors from the fact that we use interferometry data can affect our results. Since  $\Theta_b$  is a sensitive parameter according to Table 5.2a, small changes result in large errors. An issue where the beam may come into effect, is the relation between the Jy→K conversion factor. In order to perform this unit conversion, some parameters of the observing telescope needs to be assumed, including the beam size of the telescope. When integrating over an aperture,  $\Theta_b$  of the data changes and the conversion factor might not be valid beyond a certain aperture size. Even though the size of the aperture was attempted to be made as close in size to the beam as possible, there was a difference which could affect this factor. Therefore, the conversion between interferometry data to single dish equivalent values requires high accuracy to avoid the propagation of errors into the mass-loss rate.

Furthermore, the expansion velocities we have found, Table 5.1, are also consistently significantly higher (except for Y Hya), which could serve as an explanation to our higher mass-loss rates since  $v_{exp}$  is an input parameter in Equation (3.8). An increase of 50% for  $v_{exp}$ , which is almost the difference for R Hya in comparison to the literature value, leads, as seen in Table 5.2a, to an increased mass-loss rate of 21%. Clearly, this is not enough to account for our errors.

It is difficult to offer a definitive explanation for the discrepancy in  $v_{exp}$ . Since  $v_{exp}$  is defined as half of the emission line width, it is a value that follows directly from the data. Even if our assumed error in deciding the line width of  $\Delta v = 0.75 \text{ kms}^{-1}$  is underestimated by a factor of three most expansion velocities would still be higher within the margin of error than those in the literature. The literature expansion velocities for R Hya, U Hya, R For and R Crt originate from observations during 1986-1992 [5]. They mention in their discussion that the expansion velocities are uncertain due to low signal to noise and confusion with interstellar CO emission. As seen in Figure 5.1 our signal to noise is high for the CO-lines.

Therefore, it might be the case that the expansion velocities we have obtained are based on data with lower uncertainties than those in the literature, and should be given a more significant weight.

We have also noted a consistent trend in our results that a larger  $v_{exp}$  corresponds to a larger  $\dot{M}$ . This is usually what can be expected and [7] state a relationship of  $\dot{M} \propto v_{exp}^3$  while Equation (5.1) match a relation  $\dot{M} \propto v_{exp}^{0.39-0.46}$ . However, since  $\dot{M}$  depend on many variables, five stars are not enough to evaluate these relationships. All we can say is that our findings seem to agree with a larger expansion velocity leading to a larger mass-loss rate.

The difference between  $\dot{M}$  from the  $J = 2 \rightarrow 1$  and  $J = 3 \rightarrow 2$  CO transitions are for U Hya, R For and R Crt within the error margin of  $\pm 14\%$  found in Table 5.2b when we take the error for the integrated flux into account. However, for Y Hya and R Hya, this is not the case, and the mass loss-rates differ almost 50% between the largest and smallest value. Still, the values are within a factor of three as mentioned as an inherent uncertainty in the Ramstedt equation.

In conclusion, to be able to estimate more accurate mass-loss rates and to investigate the possible systematic error of higher values, analysis for more stars is needed. If larger values still are found, perhaps the conversion between interferometry and single dish data needs to be developed. Also, to reach a definite conclusion of the higher expansion velocities, analysis of the same data as the literature values are obtained from will have to be made.

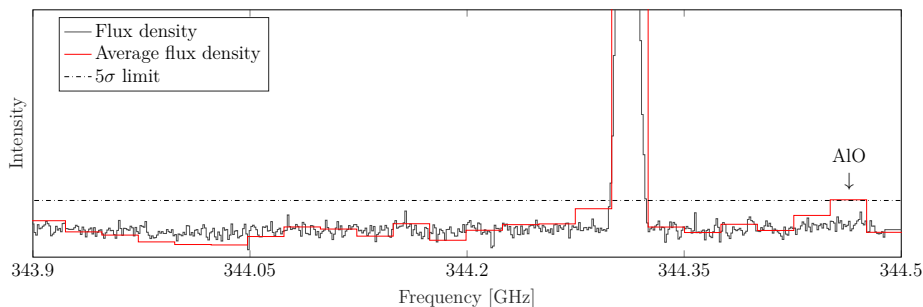
## 6.2 Identified Molecules in the CSEs

As to clarify the existence of the identified molecules for each star the results have been summarised in Table 6.1. All molecules are typically found in the CSEs of AGB stars [8, 6]. There are general differences correlating to the spectral type where the carbon-rich stars have more molecular types containing C and those in the oxygen-rich stars contain more O. In addition, the integrated flux for SiO  $J = 5 \rightarrow 4$ , which has been identified in all stars, is significantly higher for the oxygen-rich stars, as seen in Table 6.1, could indicate the difference in its abundance. These observations point to the conclusion that different spectral types have different chemical properties, which is also supported by [13].

One of the faintest emission lines that we identified was AlO. Without any signal processing methods, the line was indistinguishable from noise. However, as is shown in Figure 6.1, when averaging the flux density, the  $5\sigma$  of the noise went down, and the signal from the emission line intensified in relation. The increase in signal to noise made it possible to identify the AlO emission line at 344.463 GHz, confirming that the chosen method was suitable for finding molecules in noisy spectra.

**Table 6.1:** A summary of the molecules we identified for each star.

Molecule	Star	Carbon stars			Oxygen stars	
		Y Hya	U Hya	R For	R Hya	R Crt
CO		x	x	x	x	x
<sup>13</sup> CO		x	x	x	x	x
SiO		x	x	x	x	x
<sup>29</sup> SiO		-	-	x	x	x
HC <sub>3</sub> N		x	-	x	-	-
H <sup>13</sup> CN		x	x	x	x	x
CS		x	x	x	x	-
<sup>13</sup> CS		x	-	x	-	-
SiC <sub>2</sub>		x	-	x	-	-
<sup>13</sup> CN		-	x	x	-	-
SiS		-	-	x	-	-
SO <sub>2</sub>		-	-	-	-	x
SO		-	-	-	x	x
<sup>34</sup> SO		-	-	-	-	x
AlO		-	-	-	-	x

**Figure 6.1:** Identification of the AlO emission line. The *black solid line* is the unprocessed flux density and the *red solid line* averaged flux density. The  $5\sigma$  standard deviation of the noise is shown as the *black dot-dashed line*. For illustration purposes, the unprocessed flux density has been scaled down to have a  $5\sigma$  of the noise matching the averaged flux density.

The maser effect, outlined in Section 3.3, needs specific conditions to occur, and these conditions are not met in all parts of the CSE. Masers only occur in particular regions and for particular transitions, leading to an increased intensity. Combined with the Doppler effect, the intensity lines can be shifted in either direction effectively shifting the peak of the emission line. The shifting has to be taken into consideration when identifying the molecules as otherwise, a maser shifted line might result in the wrong identification. SiO is a common molecule which frequently displays a maser effect[23]. For R Hya to the left in Figure 6.2, the intensity peak is centred around the velocity rate of the star at  $-11 \text{ km s}^{-1}$ , as expected. However, for R Crt to the right in Figure 6.2, the line is not centred around the velocity of the star at  $11 \text{ km s}^{-1}$ . Instead, the effects of masers shift the centre of the line to a lower velocity. Looking at the frequency of the shifted intensity peak would yield a molecule different from the correct SiO  $J = 5 \rightarrow 4$  line emission. However, when comparing this emission line to possible molecules, the molecules were not reasonable to find in a CSE of

an AGB star. Together with the fact that two other transitions of SiO in R Crt has been identified we can conclude that this is a shifted SiO emission line because of the maser effect.

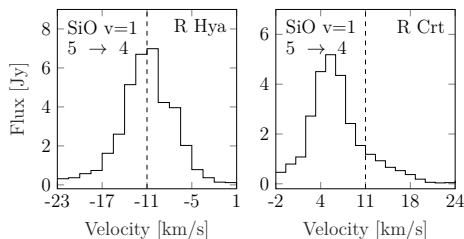


**Figure 6.2:** Emission lines of SiO  $J = 5 \rightarrow 4$  for R Hya (*left*) and R Crt (*right*) displaying the effects of a maser shifted line for R Crt. The *dotted lines* indicates the velocity at which the emission line should be centred, i.e. at the velocity of the star.

We are limited to identify molecules within the frequency ranges in Table 4.3 why there clearly are transitions and molecules we forgo. Therefore, to further study what molecules are present in our sample of stars, a broader frequency interval is necessary. Except for finding more molecules, a broader frequency range would hopefully lead to the discovery of more transitions for the already identified molecules, and would thus increase the certainty of their existence. To identify weaker transitions, either those with a lower probability for the common molecules or those of the less abundant ones, that perhaps are present within our studied frequency ranges, data with a higher signal to noise is needed. This could possibly be achieved with better knowledge of the data calibration and or the use of other observatories.

### 6.3 Continuum emission - dust

The assumed dust temperature,  $T_{dust}$ , has an exponential dependence in a black-body spectrum, Equation (3.4). Since  $T_{dust}$  can have a large range of values [24], it dominates the error for  $M_D$  and  $\dot{M}_D$ , why we limit the discussion for the errors to  $T_{dust}$ . A value of  $T_{dust} = 50$  K would for R Hya result in a dust mass one order of magnitude higher than the value given in Table 5.4 while  $T_{dust} = 450$  K would give one order lower.

As mentioned in Section 2.4.3, the gas to dust ratio can be expected to be  $\sim 1 : 100$  so using Equation (3.13) and the results for the gas mass-loss rates in Table 5.1 we can see how our results match the theory. For R For we obtain a gas to dust ratio in the order of 1:100 and for R Hya 1:1. Even though the gas to dust ratio of R For match what could be expected, the obtained ratio for R Hya gives us a further indication that our results for  $M_D$  and  $\dot{M}_D$  should not be given any significant weight. However, since  $\alpha$  deviates from 2 and the measured fluxes are higher than what is expected we can at least conclude that dust probably is present in both R For and R Hya.

In Table 5.4 we have noted that the measured flux is about half of the expected for U Hya. A possibility is that the values in the literature ( $D$ ,  $L$  and  $T$ ), which the results are based on, are uncertain. Also, the gas mass-loss rate for U Hya in Table 5.1 is the star that differs the most compared to the literature value, which could point to the same conclusion. Another possibility is that the SED of U Hya has an unusual appearance that differs from that of a black-body spectrum. No definite conclusions can be made for the continuum of U

Hya other than that it probably is not only the flux of a pure black-body spectrum that is seen in Band 6 and Band 7 since  $\alpha \neq 2$ .

The stars with  $\alpha \approx 2$ , Y Hya and R Crt, both have measured fluxes within the margin of error of 15% compared to that of the expected. Also, the calculated temperatures agree well for R Crt and are off by a margin of 200-300 K for Y Hya. Both the values of the measured fluxes and the obtained temperatures point to the conclusion that we do not see any dust for Y Hya and R Crt in Band 6 and Band 7. However, this does not mean that no dust is present in these stars, only that from our measurements, no dust is visible.

In conclusion, to obtain results with higher accuracy, more data is needed. Using only two data points (Band 6 and Band 7) produces a significant uncertainty since small errors in the measured flux propagate to large errors in  $\alpha$  and  $M_D$ . If more data is used over a broader frequency range, a SED could be fitted to the data. This would yield more details of the temperature of the stars as well as of the amount and temperature of the dust in the CSEs.

## 6.4 Closing remarks

The DEATHSTAR project has resulted in an extensive database for AGB research. Since the observations are only about a year old, there have not been many papers written on the data. However, when astronomers have made similar, although perhaps more in-depth, analyses of the stars, this thesis might be useful for comparing results.

Our results in this thesis: the obtained gas mass-loss rates together with its corresponding error analysis and evaluation of the Ramstedt equation, the expansion velocities, the identified molecules and the detection of dust, will hopefully contribute to the research of AGB stars. Knowing more of AGB stars and their important distribution of light and heavy elements to the ISM will further our understanding of the life cycle of our own as well as other galaxies.

# Bibliography

- [1] Department of Physics and Astronomy, Uppsala University, “Deathstar: Determining accurate mass-loss rates of thermally pulsing agb stars,” <http://www.astro.uu.se/deathstar/>, 2017, (Accessed on 16/5/2019).
- [2] S. Ramstedt, F. L. Schöier, H. Olofsson, and A. A. Lundgren, “On the reliability of mass-loss-rate estimates for AGB stars,” *Astronomy & Astrophysics*, vol. 487, no. 2, pp. 645–657, 6 2008. [Online]. Available: <https://doi.org/10.1051/0004-6361:20078876>
- [3] F. L. Schöier and H. Olofsson, “Models of circumstellar molecular radio line emission,” *Astronomy & Astrophysics*, vol. 368, no. 3, pp. 969–993, 3 2001. [Online]. Available: <https://doi.org/10.1051/0004-6361:20010072>
- [4] F. L. Schöier, S. Ramstedt, H. Olofsson, M. Lindqvist, J. H. Bieging, and K. B. Marvel, “The abundance of HCN in circumstellar envelopes of AGB stars of different chemical type,” *Astronomy & Astrophysics*, vol. 550, p. A78, Jan. 2013. [Online]. Available: <https://doi.org/10.1051/0004-6361/201220400>
- [5] H. Olofsson, K. Eriksson, B. Gustafsson, and U. Carlstrom, “A study of circumstellar envelopes around bright carbon stars. i - structure, kinematics, and mass-loss rate.” *The Astrophysical Journal Supplement Series*, vol. 87, p. 267, Jul. 1993. [Online]. Available: <https://doi.org/10.1086/191804>
- [6] T. Kamiński, K. T. Wong, M. R. Schmidt, H. S. P. Müller, C. A. Gottlieb, I. Cherchneff, K. M. Menten, D. Keller, S. Brünken, J. M. Winters, and N. A. Patel, “An observational study of dust nucleation in mira (o ceti),” *Astronomy & Astrophysics*, vol. 592, p. A42, Jul. 2016. [Online]. Available: <https://doi.org/10.1051/0004-6361/201628664>
- [7] S. Höfner and H. Olofsson, “Mass loss of stars on the asymptotic giant branch,” *The Astronomy and Astrophysics Review*, vol. 26, no. 1, 1 2018. [Online]. Available: <https://doi.org/10.1007/s00159-017-0106-5>
- [8] M. Maercker, “Asymptotic Giant Branch stars viewed up-close and far-off : The physics, chemistry, and evolution of their circumstellar envelopes,” Ph.D. dissertation, University of Stockholm, 2009.
- [9] A. Karakas and M. Lugaro, “The s-process in agb stars,” *Proceedings of Science*, 2010.
- [10] A. R. Choudhuri, *Astrophysics for Physicists*. Cambridge University Press, 2009. [Online]. Available: <https://doi.org/10.1017/cbo9780511802218>
- [11] J. C. Lattanzio and P. R. Wood, “Evolution, nucleosynthesis, and pulsation of AGB stars,” in *Astronomy and Astrophysics Library*. Springer New York, 2004, pp. 23–104. [Online]. Available: [https://doi.org/10.1007/978-1-4757-3876-6\\_2](https://doi.org/10.1007/978-1-4757-3876-6_2)
- [12] H. J. Habing and H. Olofsson, “AGB stars: History, structure, and characteristics,” in *Astronomy and Astrophysics Library*. Springer New York, 2004, pp. 1–21. [Online]. Available: [https://doi.org/10.1007/978-1-4757-3876-6\\_1](https://doi.org/10.1007/978-1-4757-3876-6_1)

- [13] S. Bladh and S. Höfner, “Exploring wind-driving dust species in cool luminous giants,” *Astronomy & Astrophysics*, vol. 546, p. A76, 10 2012. [Online]. Available: <https://doi.org/10.1051/0004-6361/201219138>
- [14] L. Girardi and P. Marigo, “The TP-AGB phase,” *Astronomy & Astrophysics*, vol. 462, no. 1, pp. 237–243, 10 2006. [Online]. Available: <https://doi.org/10.1051/0004-6361:20065249>
- [15] P. van Cittert, “Die wahrscheinliche schwingungsverteilung in einer von einer lichtquelle direkt oder mittels einer linse beleuchteten ebene,” *Physica*, vol. 1, no. 1-6, pp. 201–210, 1 1934. [Online]. Available: [https://doi.org/10.1016/s0031-8914\(34\)90026-4](https://doi.org/10.1016/s0031-8914(34)90026-4)
- [16] F. Zernike, “The concept of degree of coherence and its application to optical problems,” *Physica*, vol. 5, no. 8, pp. 785–795, 8 1938. [Online]. Available: [https://doi.org/10.1016/s0031-8914\(38\)80203-2](https://doi.org/10.1016/s0031-8914(38)80203-2)
- [17] M. Maercker, M. Brunner, M. Mecina, and E. D. Beck, “An independent distance estimate to the AGB star  $\rho$  sculpatoris,” *Astronomy & Astrophysics*, vol. 611, p. A102, Mar. 2018. [Online]. Available: <https://doi.org/10.1051/0004-6361/201732057>
- [18] National Radio Astronomy Observatory, “Splatalogue,” <https://www.cv.nrao.edu/php/splat/>, 7 2016, (Accessed on 16/5/2019).
- [19] L. Mattsson, H. L. Gomez, A. C. Andersen, and M. Matsuura, “From flux to dust mass: Does the grain-temperature distribution matter for estimates of cold dust masses in supernova remnants?” *Monthly Notices of the Royal Astronomical Society*, vol. 449, no. 4, pp. 4079–4090, 4 2015. [Online]. Available: <https://doi.org/10.1093/mnras/stv487>
- [20] Atacama Large Millimeter Array, “Atacama large millimeter array, data archive,” <https://almascience.eso.org/alma-data/archive>, 2 2019, (Accessed on 16/5/2019).
- [21] E. D. Beck, L. Decin, A. de Koter, K. Justtanont, T. Verhoelst, F. Kemper, and K. M. Menten, “Probing the mass-loss history of AGB and red supergiant stars from CO rotational line profiles,” *Astronomy & Astrophysics*, vol. 523, p. A18, 11 2010. [Online]. Available: <https://doi.org/10.1051/0004-6361/200913771>
- [22] J. Bergeat and L. Chevallier, “The mass loss of c-rich giants,” *Astronomy & Astrophysics*, vol. 429, no. 1, pp. 235–246, Dec. 2004. [Online]. Available: <https://doi.org/10.1051/0004-6361:20041280>
- [23] S.-H. Cho and J. Kim, “Simultaneous observations of SiO and H<sub>2</sub>O masers toward known stellar SiO maser sources,” *The Astronomical Journal*, vol. 144, no. 5, p. 129, Oct. 2012. [Online]. Available: <https://doi.org/10.1088/0004-6256/144/5/129>
- [24] E. Lagadec, D. Mékarnia, J. A. de Freitas Pacheco, and C. Dougados, “Dust temperature and density profiles in the envelopes of AGB and post-AGB carbon stars from mid-infrared observations,” *Astronomy & Astrophysics*, vol. 433, no. 2, pp. 553–564, Mar. 2005. [Online]. Available: <https://doi.org/10.1051/0004-6361:20041553>

# A

## Acronyms

⊙	The Sun
*	Star
ALMA	Atacama Large Millimeter Array
ACA	Atacama Compact Array
AGB	Asymptotic Giant Branch
DEATHSTAR	DEtermining Accurate mass-loss rates of THERmally pulsing AGB STARS
CSE	CircumStellar Envelope
CASA	Common Astronomy Software Applications
ISM	InterStellar Medium
FWHM	Full Width at Half Maxium
HR-diagram	Hertzprung–Russell diagram
MASER	Microwave Amplification by Stimulated Emission of Radiation
PEDDRO	Pulsation Enhanced Dust DRiven Outflow
RGB	Red Giant Branch
SED	Spectral Emission Distribution
ZAMS	Zero Age Main Sequence

# B

## Figures

### B.1 Emission Lines

This section presents five figures, one for each off the studied AGB stars. The figures show all identified transitions marked with their corresponding rest frequency.

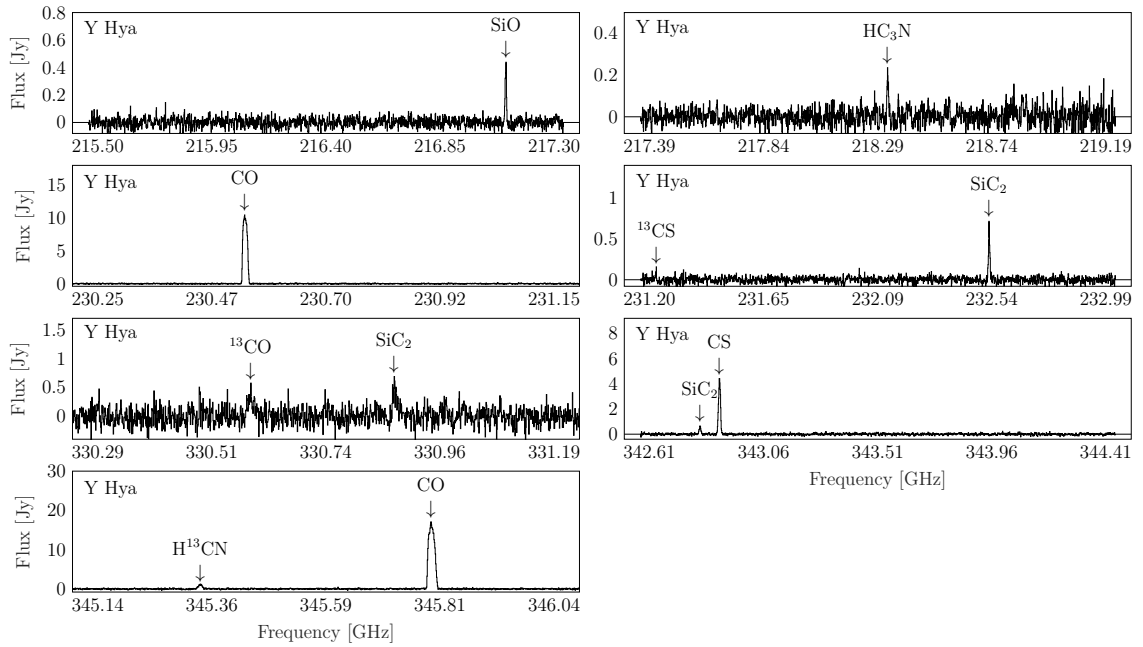


**Figure B.1:** Identified molecular transitions for the Carbon rich C-type AGB star Y Hya. The frequency spectra have been Doppler shifted.

## B. Figures

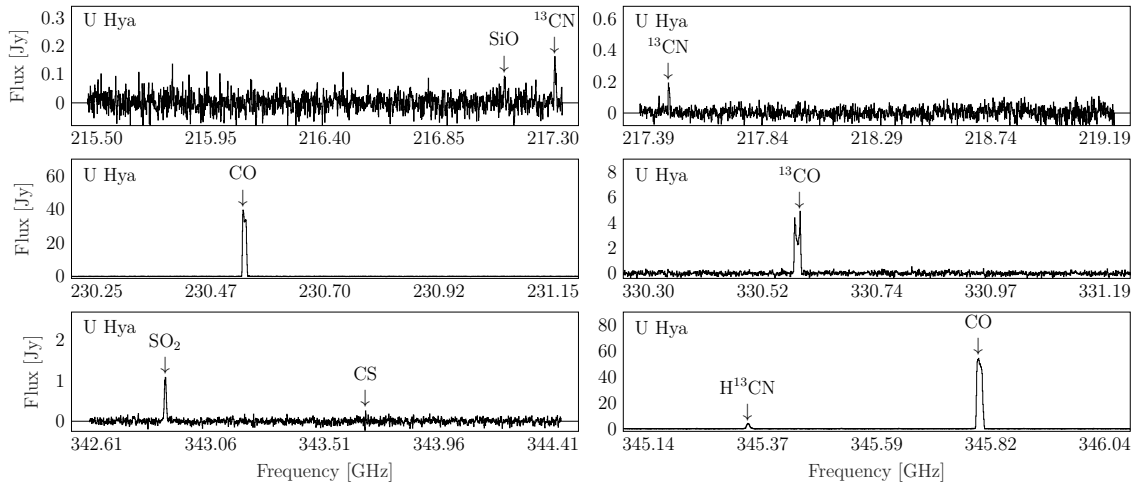


**Figure B.2:** Identified molecular transitions for the Carbon rich C-type AGB star U Hya. The frequency spectra have been Doppler shifted.

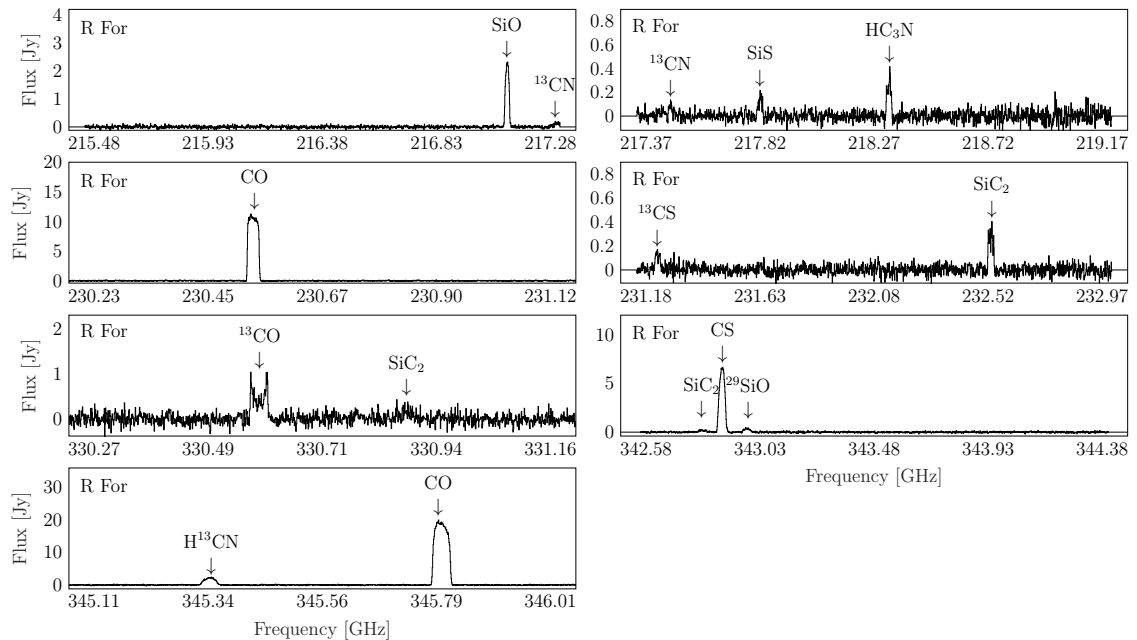


**Figure B.3:** Identified molecular transitions for the Carbon rich C-type AGB star R For. The frequency spectra have been Doppler shifted.

## B. Figures

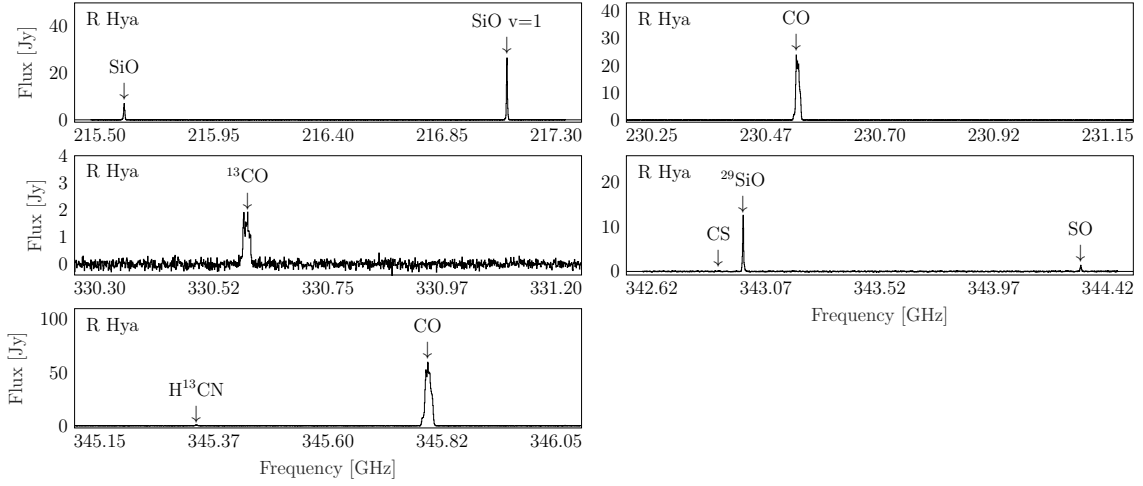


**Figure B.4:** Identified molecular transitions for the Oxygen rich M-type AGB star R Hya. The frequency spectra have been Doppler shifted.

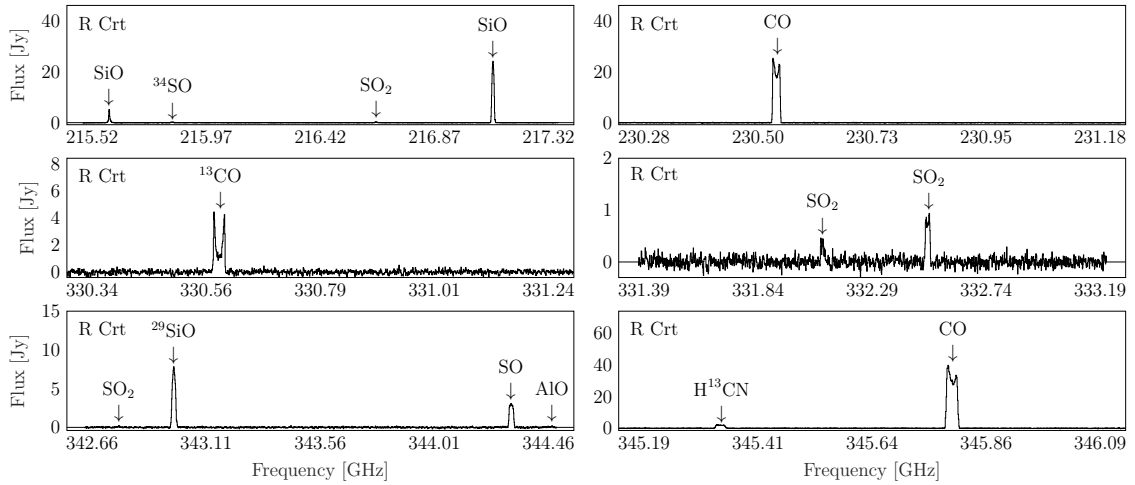


**Figure B.5:** Identified molecular transitions for the Oxygen rich M-type AGB star R Crt. The frequency spectra have been Doppler shifted.